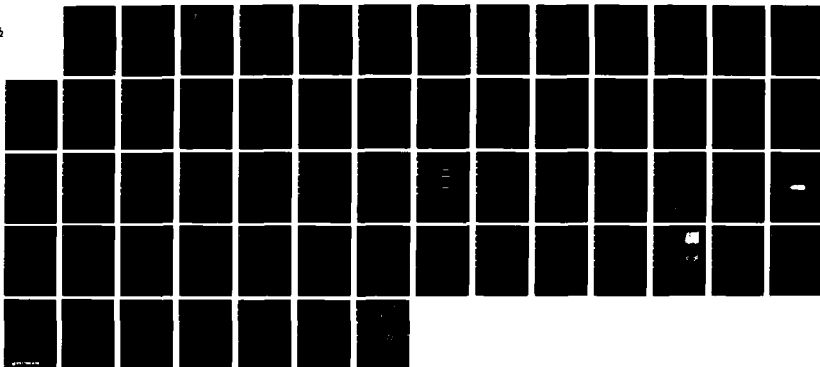


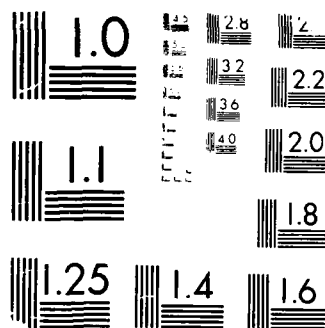
NO-A189 948 MPD (MAGNETOPLASMA DYNAMIC) THRUST CHAMBER FLOW DYNAMICS 1/1
(U) R AND D ASSOCIATES ALEXANDRIA VA 29 SEP 87
RDA-TR-144200 AFOSR-TR-87-1883 F49620-86-C-0117

UNCLASSIFIED

F/G 21/3

NL





MICROCOPY RESOLUTION TEST CHART
 NATIONAL BUREAU OF STANDARDS-1963-A

10-4116 640

AFR-TR-87-104

RDA-TR-144200

FINAL REPORT

MPD THRUST CHAMBER FLOW DYNAMICS

SEPTEMBER 1987

Prepared for:

AIR FORCE OFFICE OF SCIENTIFIC RESEARCH
BOLLING AIR FORCE BASE
WASHINGTON, DC 20332-6448

Prepared by:

RDA/WRL Staff

RDA

R & D ASSOCIATES, WASHINGTON RESEARCH LABORATORY

301A S. WEST STREET, ALEXANDRIA, VIRGINIA 22314

■ TELEPHONE: 703 684-0333

Unclassified

SECURITY CLASSIFICATION OF THIS PAGE

ADA189940

(2)

REPORT DOCUMENTATION PAGE

Form Approved
OMB No. 0704-0188

1a REPORT SECURITY CLASSIFICATION Unclassified			1b RESTRICTIVE MARKINGS		
2a SECURITY CLASSIFICATION AUTHORITY DTIC ELECTED			3 DISTRIBUTION AVAILABILITY OF REPORT Approved for public release; distribution is unlimited		
2b DECLASSIFICATION/DOWNGRADING SCHEDULE JAN 07 1988			4 PERFORMING ORGANIZATION REPORT NUMBER(S) H		
5a NAME OF PERFORMING ORGANIZATION R&D Associates, Inc.			5b OFFICE SYMBOL (if applicable) RDA/WRL		
6a ADDRESS (City, State, and ZIP Code) 301 S. West Street Alexandria, VA 22314			7a NAME OF MONITORING ORGANIZATION AFOSR/NA		
3a NAME OF FUNDING SPONSORING ORGANIZATION AFOSR/NA			3b OFFICE SYMBOL (if applicable) NA		
8a ADDRESS (City, State, and ZIP Code) Building 410, Bolling AFB DC 20332-6448			9 PROCUREMENT INSTRUMENT IDENTIFICATION NUMBER F49620-86-C-0117		
10 SOURCE OF FUNDING NUMBERS			11 TITLE (Include Security Classification) (U) MPD Thrust Chamber Flow Dynamics		
12 PERSONAL AUTHOR(S)			13a TYPE OF REPORT Annual		
13b TIME COVERED FROM 1 Oct 86 TO 30 Sep 87			14 DATE OF REPORT (Year, Month, Day) 87-09-29		
15 PAGE COUNT 57			16 SUPPLEMENTARY NOTATION		
17 COSATI CODES			18 SUBJECT TERMS (Continue on reverse if necessary and identify by block number)		
FIELD GROUP SUB-GROUP			Electric propulsion, magnetoplasmadynamic, arcjet		
19 ABSTRACT (Continue on reverse if necessary and identify by block number)					
The performance characteristics of MPD arcjets depend on proper matching of electromagnetic and fluid mechanical constraints within the thrust chamber. Experimental measurements of internal flow conditions during MPD arcjet operation are needed to guide development of flow models and to assess the validity of theoretical predictions. Efforts are continuing at the RDA Washington Research Laboratory, in a cooperative effort with an AFOSR-sponsored MIT group to apply an array of diagnostic techniques including time-, space-, and spectrally-resolved photography, to examine MPD arcjet internal flows. Experimental elucidation of the internal flow structure is used to develop predictive models for optimal geometries and operating parameters. As part of the modeling effort, for example, probes have been used to map the current and voltage distributions within					
20 DISTRIBUTION AVAILABILITY OF ABSTRACT <input checked="" type="checkbox"/> UNCLASSIFIED/UNLIMITED <input checked="" type="checkbox"/> SAME AS RPT <input type="checkbox"/> DTIC USERS			21 ABSTRACT SECURITY CLASSIFICATION Unclassified		
22a NAME OF RESPONSIBLE INDIVIDUAL Dr Mitat Birkan			22b TELEPHONE (Include Area Code) (202) 767-4937		
			22c OFFICE SYMBOL AFOSR/NA		

19. (continued)

uniform height and flared annular channels. This work is concerned with the effect of thruster channel variations on the current conduction region of the MPD internal flow. Other aspects of the internal flow structure that have been modeled in the past year involve the transition of the input mass flow from neutral gas to electrically-conducting plasma. Scale sizes for the transition region have been estimated in terms of the electrical and thermodynamic properties of the propellant gas (e.g., argon). These estimates indicate that the electrical conductivity of the flow can be established in distances that are small compared to the characteristic dimension for current conduction near the entrance to the arcjet thrust chamber. Comparison of convection versus thermal conduction suggests that heat conduction (and associated surface ablation) may become more important at higher exhaust speeds. Examination of the mass injection region will be an important area for experimental work in the next year, particularly in regard to processes near the injectors that can affect thruster lifetime.

SEPTEMBER 1987

ANNUAL REPORT

MPD THRUST CHAMBER FLOW DYNAMICS

Prepared for:

Air Force Office of Scientific Research
Bolling Air Force Base
Washington, DC 20332-6448

Prepared by:

RDA/WRL Staff



Accession For	
NTIS GFA&I	<input checked="checked" type="checkbox"/>
DTIC TAB	<input type="checkbox"/>
Unannounced	<input type="checkbox"/>
Justification	
By	
Distribution	
Availability	
Availability /OL	
Dist	
Dist	

A-1

TABLE OF CONTENTS

	PAGE
LIST OF ILLUSTRATIONS	ii
NOMENCLATURE	iv
I. SUMMARY	1
II. BACKGROUND	3
III. APPROACH	5
IV. PROGRESS	7
V. CONCLUDING REMARKS	18
VI. LIST OF REFERENCES	20
VII. APPENDICES	21
I. Details of Spectroscopic Analysis System	22
II. Effect of Axial Variation of Electrode Spacing on MPD Arcjet Behavior	36
III. Critical Speed and Voltage-Current Characteristics in Self-Field Plasma Thrusters	46

LIST OF ILLUSTRATIONS

FIGURE	PAGE
1. Electrical conductivity <u>vs</u> position in the transition region, in terms of the resistive heat integral $H(T)$, for argon.	12
2. Normalized electrical conductivity (with σ_0 defined by equation (13)) <u>vs</u> normalized position α . Initial conditions for this solution are $s = 0.1$ in the main discharge (corresponding to argon at 20,000 °K) and zero heat flux at that position.	16
I-1. SIT camera observed counts (vertical axis) <u>vs</u> relative input light flux (horizontal axis) at two horizontal rows shows good spatial uniformity of responsivity and linear response to 600 counts.	25
I-2. Relative system spectral response between 400 and 800 nm normalized to 1.0 at 700 nm as measured by calibrated tungsten filament lamp.	25
I-3. Visual representation of SIT camera data of an argon arcjet. Each SIT camera data frame contains information in three dimensions: spectral, spatial, and intensity.	26
I-4. Intensity <u>vs</u> wavelength of Figure I-3 at row 55 (approximately 0.85 cm from arcjet centerline) shows emission from argon ions at 460.956 nm (center), 457.90 nm (center right) and 457.935 nm (right).	27
I-5. Relative intensity <u>vs</u> wavelength of 727.293 nm neutral argon emission at 2 cm from exit plane of an argon arcjet.	28
I-6. Integrated spatial intensity profile of emission line shown in Figure I-5. (a) Raw intensity spatial profile; (b) Digitally-smoothed to remove high spatial frequencies characteristic of shot noise.	30
I-7. Abel inversion of digitally-smoothed integrated argon emission shown in Figures I-5, I-6a and I-6b yield spatially-resolved spectral line emissivity.	31

FIGURE	PAGE
I-8. Visual representation of 656.285 nm hydrogen emission 2 cm downstream of arcjet exit as observed by SIT camera system. Analysis of hydrogen spectral emission profile yields spatial electron density.	32
I-9. Intensity <u>vs</u> wavelength of 656.285 nm hydrogen emission 2 cm downstream of arcjet exit at one spatial location.	33
I-10. Spectral emission line profile of 656.285 nm hydrogen emission from data at 2 cm downstream of an argon arcjet exit plane (1.6% hydrogen added to argon).	34
I-11. Spatial emission profile along 656.285 nm hydrogen emission peak from data at 2 cm downstream of an argon arcjet exit plane (1.6% hydrogen added to argon).	35

Nomenclature

A	cross-sectional area for propellant mass flow
B	maximum magnetic induction field level
C_c	coefficient in formula for electrical conductivity
C_k	coefficient in formula for thermal conductivity
E	electric field
f	geometric factor for electric field
$F(s)$	function of normalized electrical conductivity, s
G	geometric factor based on arcjet design
g	geometric factor in arcjet thrust formula
H	integral of the product of electrical conductivity and specific heat over temperature
H_f	value of H at operating conductivity level, $\sigma(T_f)$
J	total current
j	current density
K	thermal conductivity
K_0	characteristic value of K
L	channel length
\dot{m}	propellant mass flow rate
\dot{m}_a	mass flow rate per unit area
R_m	magnetic Reynolds number
r	radial position
r_a	anode radius
r_c	cathode radius
T	temperature
t	time
u	flow speed
u_E	exhaust speed
w	ratio of C_k/C_c
x	streamwise displacement
x_0	characteristic scale for heat conduction
α	normalized displacement, x/x_0
Δ	distance over which electrical conductivity established
μ	permeability of free space
ρ	mass density
σ	electrical conductivity
σ_0	characteristic value of σ

I. SUMMARY

The magnetoplasmadynamic (MPD) arcjet has been recognized over the last decade and a half as a prime candidate for high thrust density, high specific impulse missions, such as spacecraft orbital maneuvering. Since the performance characteristics of MPD arcjets depend on proper matching of electromagnetic and fluid mechanical constraints within the thrust chamber, theoretical modeling of the internal flow dynamics is presently under development. Experimental measurements of internal flow conditions during MPD arcjet operation are needed to guide development of flow models and to assess the validity of theoretical predictions. Presently, some theorists have been referring to data obtained by Turchi in 1970 applying rudimentary diagnostic techniques to a quasi-steady MPD arcjet of non-optimum design (i.e., short cathode, ablating insulator, poorly-mixed propellant feed). New measurements are needed using modern diagnostics in MPD arcjet flows that should be more nearly optimal (based on the last fifteen years of development).

At the RDA Washington Research Laboratory, in a cooperative effort with the AFOSR-sponsored MIT group under Prof. Martinez-Sanchez, an array of diagnostic techniques has been assembled, including time-, space-, and spectrally-resolved photography, with which to examine MPD arcjet internal flows. In addition, the previous arcjet operating pulsetime at RDA has been extended from 150 μ sec to the millisecond regime appropriate for studies of megawatt quasi-steady and steady MPD arcjets. The power and mass flow feed systems have been redesigned and rebuilt to accommodate a variety of MPD arcjet geometries ranging from large cathode-diameter annular channels with axial variation of transverse dimension to channels formed by nested biconical electrodes.

Efforts are continuing to apply the assembled apparatus and diagnostic tools to measure the electromagnetic and plasma flow conditions in MPD arcjets. Experimental elucidation of the internal flow structure will then be used to develop predictive

models for optimal geometries and operating parameters. As part of the MIT modeling effort, for example, probes have been used to map the current and voltage distributions within uniform height and flared annular channels. This work is concerned with the effect of thruster channel variations on the current conduction regions of the MPD internal flow. Other aspects of the internal flow structure that have been modeled in the past year involve the transition of the input mass flow from neutral gas to electrically-conducting plasma. Scale sizes for the transition region have been estimated in terms of the electrical and thermodynamic properties of the propellant gas (e.g., argon). These estimates indicate that the electrical conductivity of the flow can be established in distances that are small compared to the characteristic dimension for current conduction near the entrance to the arcjet thrust chamber. Comparison of convection versus thermal conduction suggests that heat conduction (and associated surface ablation) may become more important at higher exhaust speeds. Examination of the mass injection region will be an important area for experimental work in the next year, particularly in regard to processes near the injectors that can affect thruster lifetime.

II. BACKGROUND

Over the past two decades, a large number of studies have been performed in which MPD arcjet operating parameters (e.g., current and mass flow rate) are changed and variations in arcjet behavior are measured. The effects on thruster performance of parameter variations, including overall electrode and injector geometry changes, have also been noted. The basic problem is that the flow field and electromagnetic structures within the MPD thrust chamber can change significantly as operating conditions are varied, so differences in performance may include different physical interactions between the internal flow and the arcjet geometry. Such differences in physical interaction include, for example, enhanced viscous effects along the cathode (center conductor) at higher currents and lower mass flow rates simply because the current pattern has a greater axial component (due to Hall effect and higher magnetic Reynolds number) so the internal flow is directed radially inward to a greater degree. The relationship of the mass injector positions to the electrode surfaces also changes as variation of overall operating values changes the directions of current density and acceleration patterns.

The limited theoretical understanding of the MPD arcjet and its beginnings as a fortuitously discovered mode of an electro-thermal arcjet have tended to freeze the electrode configuration in forms that are unlikely to be ideal. To improve the MPD arcjet configuration and operating conditions, however, guidance is required in regard to the effects of geometry and terminal parameters on internal processes and structures. Recent theoretical work¹, under separate AFOSR funding, by the MIT group led by Martinez-Sanchez indicates that proper tailoring of the transverse dimensions of the thrust chamber and the distribution of electrode potential can provide more uniform current distribution and possibly improved performance of MPD arcjets. Such theoretical effort needs to be benchmarked by experiments in appropriate geometries.

The cathode region of an MPD arcjet was mapped in 1970 by Turchi using magnetic and electric field probes². The electron temperatures were determined, along with electron density, by Langmuir probe techniques. On the basis of this diagnostic work, Turchi analyzed the electromagnetic and flow structure of the plasma. That this rudimentary work, carried out 15 years ago, is still used as a basic source by people seeking to model the MPD arcjet suggests the need for improved measurements with modern diagnostic techniques. Furthermore, the MPD thruster in which this work was done is, by present standards, a non-ideal configuration. The cathode was quite short, the gas flow ports were poorly arranged, and the anode was essentially a ported planar disc. Useful results were obtained with electric and magnetic measurement techniques, but the Langmuir probe results for temperature and density were less reliable. (Modern spectroscopic diagnostics are much more appropriate.) Plasma flow characteristics were inferred by Turchi using the two-fluid MHD equations. These measurements could be made in a direct manner using Doppler and spectroscopic techniques. Computerized data handling now allows ready manipulation of a large number of such measurements, so complete examination of the MPD thruster internal flow should be possible.

III. APPROACH

There are two parts to the present program to develop a useful understanding of MPD arcjet internal flow dynamics. Theoretical models are created that predict relationships between external arcjet variables (e.g., geometry, current, mass flow) and internal structures (e.g., current conduction zones, boundary layers, sheaths). Experimental techniques can then be applied to examine the fluid mechanical and electromagnetic structure of the MPD arcjet internal flow in order to validate and/or encourage theoretical modeling.

Probes are still useful tools and can be employed to map the current and voltage distributions in the arcjet. Framing camera photographs taken axially and through view ports in the outer electrode can be used for survey work and to identify flow aberrations (such as asymmetries). The electron density in some regions at least may be deduced from spectroscopically-measured Stark broadening of selected spectral lines. Temperatures can also be measured using line intensity ratios and flow velocities may be obtained from Doppler shifts of spectral lines. In this way, data can be obtained on flow fields for comparison with the results of calculations using two-fluid magnetohydrodynamic theory. The experimental program and cross-check with theory could be carried out for a variety of arcjet configurations including uniform and flared channel devices and for varying conditions of current and mass flow as appropriate to test theoretical understanding (rather than empirically to improve thruster performance). For example, the fuel mass flow can be reduced to provoke "onset" conditions and the electromagnetic and flow characteristics of the internal flow associated with this mode of behavior can be examined directly. Models for the MPD arcjet internal flow are extended and developed by using the experimental results to delineate important physical processes, such as Hall effect and viscous coupling to electrodes that might otherwise be ignored by initial modeling attempts. It is likely that two-dimensional MHD computer codes will be needed to

calculate the basic flow accurately, but one-dimensional models with perturbation techniques (e.g., developed by the MIT group) can provide useful insights when combined with experimentally-determined regimes and modes of interest.

IV. PROGRESS

During the first year of the present effort, activities have included significant improvement of the facilities and diagnostics needed for the experimental program, detailed examination of the electromagnetic structure in several MPD arcjet systems, and development of models for internal flow structures. These activities have been a cooperative effort by the RDA Washington Research Laboratory and the MIT group under Prof. M. Martinez-Sanchez, under separate AFOSR sponsorship.

Experimental Efforts

In this cooperative effort, the power supply was upgraded from a 20 kJ, 150 μ sec pulse forming network to a 400 kJ, 0.5-1 msec LC-ladder style pulseline. Appropriate changes in the current transmission lines and coupling to the arcjet chamber and in the arcjet electrical feed were also accomplished. The arcjet feed design allows several types of arcjets to be tested without changing the basic power and gas handling connections. In addition, the gas feed was upgraded to match better to the higher currents (50 kA vs 12 kA) provided by the new power source.

In addition to probe techniques, optical diagnostics have been developed and improved. Spatial distributions of electron density have been determined by measuring the Stark broadening profiles of the observed emission lines. With the same spectroscopic system, plasma flow velocities will be obtained from measurement of the Doppler shift of spectral lines. The spectral analysis system now available can measure a shift of 0.006 nm using third order Ar II line, which implies a minimum detectable velocity of approximately 3700 m/s. Plasma electron temperature will be determined by the Boltzmann plot technique in which relative intensities of spectral lines are compared.

To enable spectroscopic analysis of the entire flow field, a digital spectral and spatial data acquisition system has been

developed comprising a 1.2 meter, $f/11.5$ spectrograph with a EG&G/PARC intensified optical multichannel analyzer (SIT camera). The spectral and spatial output from the camera is processed by an IBM System 9000 laboratory computer for immediate background subtraction and signal averaging. Extensive computer software is available to smooth the data, perform background subtraction, and line intensity integration. An Abel inversion routine can then be used to yield line profile measurements or spectral line intensities for the axisymmetric plasma flow. A more detailed description of the digital spectral and spatial data acquisition system is provided in Appendix I.

Large diameter, annular arcjets have been attempted in order to achieve better comparison with theoretical models that do not include cylindrical effects. The length of the channel has been adjusted and the total current increased to obtain acceptable discharge uniformity. Flared channels have been compared with channels of uniform height (interelectrode gap vs axial position) to check theoretical predictions of current density distributions. Evidence of substantial axial current in the flow (Hall effect) indicates the need for additional modeling activity. Preliminary results of experiments with large diameter annular arcjets were presented at the 19th International Electric Propulsion Conference (Appendix II). More detailed examination will be the subject of a doctoral dissertation by D.J. Heimerdinger (to be reported separately under AFOSR-sponsorship).

Theoretical Efforts

In a self-field magnetoplasdynamic arcjet, the main structure of the discharge is governed by the competition between convection and diffusion of magnetic flux. For high magnetic Reynolds number, $R_m = \sigma \mu_0 U L$, this competition favors convection and can result in a bifurcated current distribution. The current density is highest in regions near the entrance and exit of the MPD channel, where the back electromotive forces (EMF) are lowest, (at the entrance because the flow speed is low, and at the exit because the magnetic field must decrease to zero).

Analysis¹ based on high magnetic Reynolds number flow, $R_m \gg 1$, suggests that the axial distribution of current can be controlled by varying the interelectrode gap along the channel. Other work² utilizes the magnetic Reynolds number to scale the axial thickness of the main current conduction regions of the channel, thereby obtaining a relationship between heat generation (due to resistive dissipation) and thrust power. This relationship is then used to examine the behavior of high power MPD arcjets in terms of voltage-current characteristics and possible exhaust velocity limitations (Appendix III).

It is assumed in the preceding analyses that the plasma flow has achieved a sufficient (and uniform) electrical conductivity to justify the high R_m approximation. The initial temperature of the propellant mass flow, however, as it enters the MPD thruster is low (\approx room temperature) so its electrical conductivity is negligible. It is useful to consider the transition of the propellant flow from very low to high conductivity due to resistive heating. Since the geometry of the injector region may place this transition region electrically in parallel with the MPD discharge flow, a connection might be expected between the propellant electrical and thermodynamic properties and the overall power distribution in the arcjet. A sub-structure of the discharge flow at the MPD channel entrance can be delineated, perhaps resembling the flame zone in propellant combustion. The size of this structure may be compared with the dimensions for other processes to suggest possible consequences for MPD arcjet operation.

Current Integral Approach

In the analysis of electrically-exploded metallic fuses, such as wires or foils, it is common to invoke the change in electrical properties with change in thermodynamic state of the fuse material.³ Typically, the operation of high power fuses occurs on a time short compared to that required for heat transfer (as opposed to lower power fuses that follow Preece's law⁴). The temperature and state of the fuse thus depends on the

heat deposited by resistive dissipation:

$$\frac{j^2}{\sigma} dt = \rho c dT \quad (1)$$

where σ = electrical conductivity, j is the instantaneous current density, ρ = mass density, c = heat capacity per unit mass, and the elapsed time and temperature increase are respectively, t and T . For many materials, under a range of conditions, the electrical conductivity will be a function of temperature. Equation (1) can then be rearranged to form the so-called current integral:

$$\int j^2 dt = \int \sigma \rho c dT \quad , \quad (2)$$

where the right-hand side depends only on material properties and may be integrated between particular states, such as room temperature to vaporization. The left-hand side does not depend on the instantaneous circuit current, J , but may be adjusted by choosing the cross-sectional area of the fuse to achieve a current density, j , such that integration over the circuit waveform provides the desired fusing action after a specified time. Fuses designed in this manner have been quite successful in a variety of experiments.⁵

Near the entrance to the MPD channel, where the flow velocity is much lower than the eventual exhaust speed, it is possible to apply the current integral approach to convecting fluid elements and thereby estimate the distance required to achieve high electrical conductivity. If heat transfer and conversion of thermal energy to kinetic energy are neglected as initial approximations, then a fluid element of fixed mass will experience a temperature increase due to resistive heating as it enters the main discharge region:

$$\rho c_p dT = \sigma E^2 dt \quad (3)$$

where E is the electric field across the main discharge. This electric field, in a steady or quasi-steady arcjet, must also be supported by the propellant flow (downstream of the injector plate) as it approaches and enters the main discharge.

The time spent by the fluid element at any position x to $x + dx$ is merely $dt = dx/u$, where u is the flow speed at that point. The local flow speed, however, may be written in terms of the mass flow per unit area \dot{m}_a and the local mass density $u = \dot{m}_a/\rho$, so

$$\frac{E^2}{\dot{m}_a} dx = \frac{c_p}{\sigma} dT \quad . \quad (4)$$

For a one-dimensional flow \dot{m}_a is independent of x , so integration of equation (4) provides a distance Δ proportional to an integral of flow properties over the temperature interval:

$$\Delta = \frac{\dot{m}_a}{E^2} \int \frac{c_p}{\sigma} dT \quad . \quad (5)$$

This calculation is completely analogous to that for the exploding fuse, with the caution that the conductivity and specific heat of a partially ionized gas are not functions simply of temperature; in the range of 0.5 to 2 eV, however, calculated properties of argon,^{6,7} for example, suggest that the ratio of enthalpy to conductivity only varies by about a factor of two for a pressure variation of two orders of magnitude (0.01 to 1. atmospheres). The present discussion is primarily concerned with scaling of discharge structures, which should not be obscured by absolute values that will vary with the detailed flow chemistry.

The resistive heat integral

$$H(T) = \int \frac{c_p}{\sigma} dT \quad (6)$$

is displayed in Figure 1 as the scaled thickness $E^2 \Delta / \dot{m}_a = H(T)$ vs the electrical conductivity σ . An order of magnitude decrease in

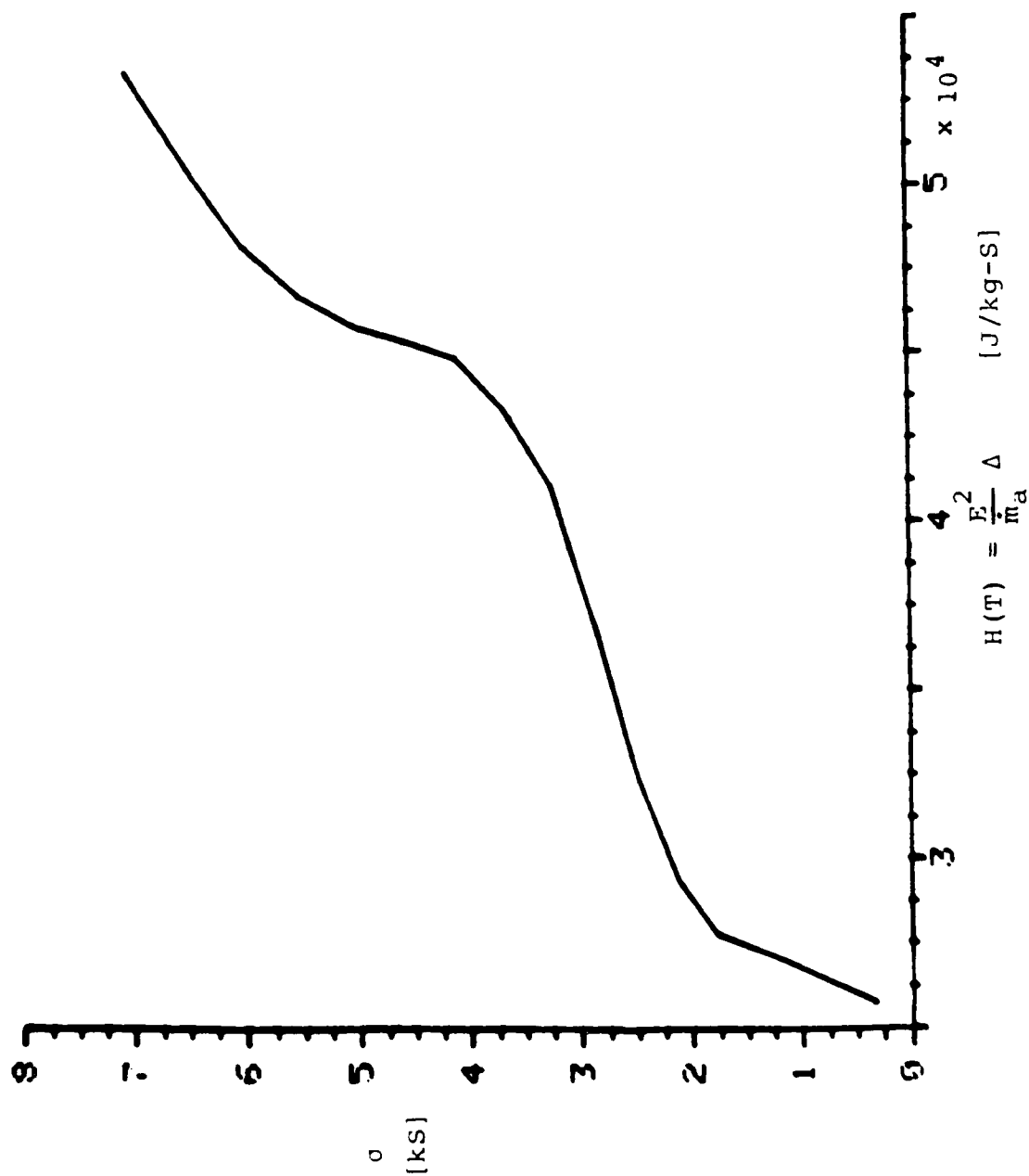


Figure 1. Electrical conductivity vs position in the transition region, in terms of the resistive heat integral $H(T)$, for argon.

conductivity occurs from $T = 20,000^\circ \text{ K}$ down to $T \approx 6,000^\circ \text{ K}$, and thereby defines the effective thickness of the transition region between non-conducting and highly conducting flow. With numerical values typical of experimental operation ($E = 3500 \text{ V/m}$ and $\dot{m}_a = 0.5 \text{ kg/m}^2\text{-s}$), the actual transition region thickness for argon would be about 1 mm, which is much less than the characteristic discharge thickness based on the magnetic Reynolds number ($\delta = 1/\sigma\mu u_E \approx 1 - 2 \text{ cm}$).

Scaling of the Transition Region

For a given value $H_f = H(T_f)$, corresponding to the full operating conductivity of the MPD flow, the size of the transition region will depend on the electric field established across the main discharge. This electric field is directly related to the back EMF in the high magnetic Reynolds number flow, which scales as the product of exhaust speed u_E and magnetic field B . Thus:

$$E = fu_E B \quad (7)$$

where the value of f depends on the geometry of the thruster; (since u_E and B are the maximum values of these quantities in the flow, f will be less than unity, but must also be adjusted to correspond to the appropriate electric field at the radius of the mass flow injection). The transition thickness is then:

$$\Delta = \frac{\dot{m}_a H_f}{f^2 u_E^2 B^2} \quad (8)$$

The maximum magnetic field is proportional to the total current

$$B = \frac{\mu J}{2\pi r} \quad (9)$$

and the exhaust velocity for the MPD thruster, based on electromagnetic forces may be written as

$$u_E = \frac{\mu J^2}{4\pi} \frac{g}{\dot{m}} \quad (10)$$

where g is a factor depending on the geometry of the thruster, for example $g = (\ln r_A/r_C + 3/4)$, based on the ratio of anode and cathode radii r_A/r_C . Note that the full mass flow $\dot{m} = \dot{m}_a A$ is utilized here. Substitution and rearrangement of terms in equation (8) then provides:

$$\Delta = \frac{G H_f}{u_E^3} \quad (11)$$

The factor G includes all the previous terms related to the thruster geometry (and also other physical constants).

Equation (11) indicates that the transition thickness decreases rapidly with increased exhaust speed. In fact, since the main discharge thickness scales as u_E^{-1} , the transition region becomes a progressively smaller portion of the discharge as J^2/\dot{m} increases. With the earlier numerical estimate indicating a transition thickness that is less than ten percent of the magnetic Reynolds number thickness, it appears that approximating the MPD flow with a uniform, high electrical conductivity is indeed valid for the entrance region. Even though the main discharge thickness decreases with higher magnetic Reynolds number, the establishment of a high conductivity flow occurs on still smaller dimensions. A limit to this benign situation occurs, however, due to heat conduction.

Thermal Conduction in the Transition Region

As the dimension of the transition region decreases, the temperature gradient in the flow increases. At some point, the initial model in which resistive dissipation simply increased the flow temperature becomes totally inadequate. It is useful to examine the opposite limit, namely, a balance between heat conduction and resistive dissipation:

$$\frac{\partial}{\partial x} \left(K(T) \frac{\partial T}{\partial x} \right) + \sigma(T) E^2 = 0. \quad (12)$$

Both the thermal conductivity $K(T)$ and the electrical conductivity are rapidly varying functions of temperature in the transition region. Inspection of the behavior of thermal and electrical conductivity as functions of temperature and pressure, calculated in Ref 7, suggests that in the transition region the following forms may be adequate for the present discussion.

$$K = K_0 e^{-C_K/T} \quad \text{and} \quad \sigma = \sigma_0 e^{-C_C/T} . \quad (13)$$

Such formulation allows the simplification:

$$\frac{K}{K_0} = \left(\frac{\sigma}{\sigma_0} \right)^w \quad (14)$$

where $w = C_K/C_C$, reflecting the typical situation that good electrical conductors are good thermal conductors. Equation (12) may then be nondimensionalized in terms of normalized variables

$$\alpha = x/x_0 \quad , \quad s = \sigma/\sigma_0 \quad (15)$$

so that

$$\frac{\partial}{\partial \alpha} \left[\frac{s^{w-1}}{(\ln s)^2} \frac{\partial s}{\partial \alpha} \right] = - \left[\frac{\sigma_0 E^2 x_0^2}{K_0 C_C} \right] s . \quad (16)$$

With $F(s) = s^{w-1}/(\ln s)^2$, this equation simplifies to:

$$\frac{\partial}{\partial \alpha} \left[F(s) \frac{\partial s}{\partial \alpha} \right] = -s \quad , \quad (17)$$

when the characteristic distance for change in electrical conductivity is identified as:

$$x_0 = \left[\frac{K_0 C_C}{\sigma_0} \right]^{1/2} / E . \quad (18)$$

In Figure 2, a solution of Equation (17) is displayed for the case of $s = 0.1$ in the main discharge. Note that an order of magnitude change in electrical conductivity requires a distance of about $2x_0$. To match equation (13) to the results in Ref 7, appropriate values for the transition region in an MPD arcjet using argon would be $K_0 = 5 \text{ w/m}^\circ\text{K}$, $\sigma_0 = 1.5 \times 10^5 \text{ mho/m}$, and

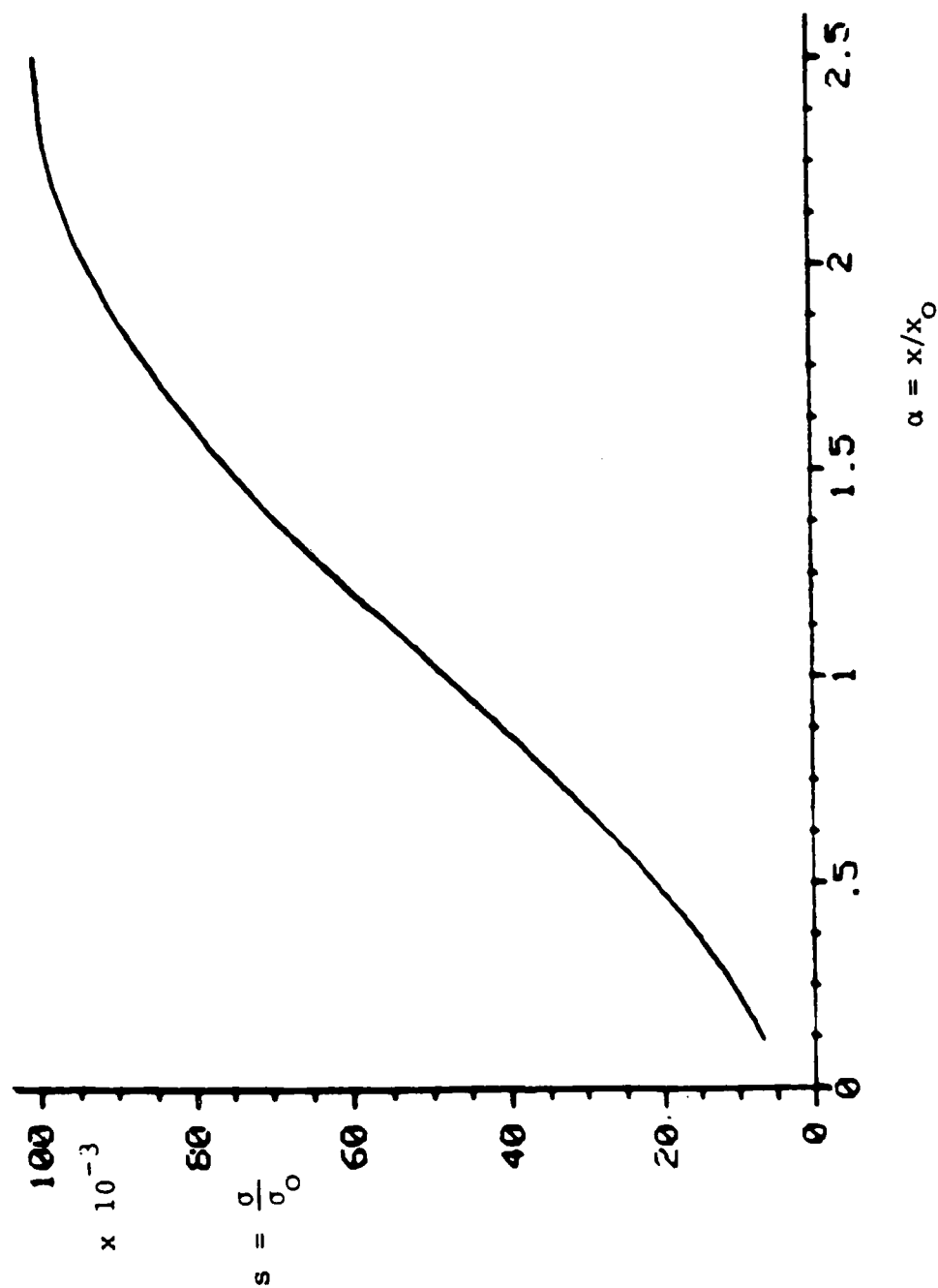


Figure 2. Normalized electrical conductivity (with σ_0 defined by equation (13)) vs normalized position α . Initial conditions for this solution are $s = 0.1$ in the main discharge (corresponding to argon at 20,000 °K) and zero heat flux at that position.

$C_c = 4.6 \times 10^4$ °K. For $E = 3500$ V/m, as before, the characteristic scale size below which thermal conduction will tend to prevent resistive heating of the input mass flow to high conductivity is then $x_0 = 0.3$ mm. At the specified value of electric field, $x_0 < \Delta$, but a factor of two increase in electric field (at fixed m_a) could reverse this inequality.

In summary, it appears that the size of the transition region is much smaller than typical MPD discharge dimensions, but could become comparable to gradient scales for heat conduction as the electric field supported by the discharge increases with higher exhaust velocity. Such higher velocity operation reduces the thickness of the MPD discharge, increasing resistive dissipation.² Perhaps more importantly, it allows the high temperature, high conductivity working fluid to be generated closer to the injection region. This proximity increases the heat conduction to cold boundaries removing energy that would otherwise be used more efficiently to create the plasma flow. In some instances, the increased heat flux will cause surface ablation, resulting in longterm thruster degradation and lower exhaust speeds (as discussed in Ref 2). Higher power operation can thus result in less performance than anticipated because of increased heat transfer and its consequences. Since the transition region electrically shunts the MPD discharge, more detailed study of the injector region is probably warranted in order to understand the effects of injector and backplate design on MPD arcjet behavior.

V. CONCLUDING REMARKS

Consideration of the MPD arcjet internal flow from a quasi-one dimensional standpoint provides structural details that manifest the competition among processes of convection and diffusion. The current density distribution for an acceleration channel of uniform transverse dimension will tend to bifurcate into high current density regions at the entrance and exit of the channel. The latter concentration in a one-dimensional formulation depends on the requirement of zero magnetic field at the end of the channel. This requirement is artificial for a real MPD accelerator exhausting into vacuum, and may be replaced by two-dimensional flow regions extending from the edges of the channel exit. In the high magnetic Reynolds number limit (at high density), these regions (for rectangular geometry) are centered-expansion fans, with characteristic lines corresponding to current streamlines. Current concentrations thus occur at both electrode edges (for a rectangular, parallel-plate accelerator). In coaxial geometry, there is a current concentration along the inside diameter of the anode orifice, and also downstream of the end of the cathode (where the radially-inward expansion of the annular MPD flow corresponds to a non-simple region of interacting expansion fans and reflected compression waves).

The current concentration at the entrance to the MPD thruster occurs where the electrically-conducting flow has a relatively low speed (and thus acts as a low-impedance shunt across the linear electric motor represented by the thruster). Magnetic field can diffuse into this low speed flow before subsequent acceleration increases the flow speed sufficiently to convect magnetic flux downstream. A scaling analysis (Appendix III) indicates that higher flow speed increases the current concentration at the entrance resulting in greater resistive dissipation and increased heat transfer to the arcjet electrodes and back plate. As a first step in examining the energy transport near the arcjet entrance, the transition of the input mass flow from neutral gas to electrically-conducting

plasma was modeled during the past year. Further work needs to be done to consider the mass injection region in two (and possibly three) dimensions in order to understand properly the upstream boundary conditions that this region may provide in overall MPD arcjet operation, performance and lifetime. Detailed experimental examination of the injector region will be very important in developing appropriate models. (Older works at Princeton by Turchi with probes and spectroscopically by A. Bruckner⁹ indicate that near the injectors there are several interesting features that can be successfully diagnosed.)

Since the overall flow field within the MPD arcjet thrust chamber is not quasi-one dimensional, the placement of the mass injectors relative to the current distribution can change as current and mass flow values are varied. Thus, the effective geometry of the device changes with operating conditions and must be measured (spectroscopically and with probes) in order to understand arcjet behavior. The MPD flow regime may be inherently two-dimensional, so the need to establish by experimental diagnosis the flow structure for each set of operating conditions is probably unavoidable.

The two-dimensionality of the MPD flow field further complicates comparison of experimental and theoretical results because simple solutions appropriate to the basic internal flow do not exist. (For example, in the MPD regime, there is a significant axial component to the current, so the main flow is accelerated to high Mach numbers at finite angle of attack onto the cylindrical blunt body represented by the arcjet cathode.) Development and application of two-dimensional MHD code techniques will be necessary in order to progress beyond qualitative guidance in the design of MPD arcjets. Some work has started in this direction at MIT, under AFOSR-sponsorship. On other research programs, RDA/WRL has been closely involved with two-dimensional MHD codes for coaxial plasma guns (AFWL) and dense plasmajets (AFOSR/SDIO), so there may be opportunities to apply existing capabilities to the MPD arcjet problem.

VI. LIST OF REFERENCES

1. Martinez-Sanchez, M. and Heimerdinger, D.J., "Two-Dimensional Analysis of an MPD Arcjet," AIAA-85-2040. Presented at 18th International Electric Propulsion Conference, Sept 30-Oct 2, 1985, Alexandria, VA.
2. Turchi, P.J., "The Cathode Region of a Quasi-Steady Magneto-plasmadynamic Arcjet," Department of Aerospace and Mechanical Sciences, Princeton University, Princeton, NJ, Rept. AMS 940T, September 1970.
3. Turchi, P.J., "Critical Speed and Voltage-Current Characteristics in Self-Field Plasma Thrusters," Journal of Propulsion and Power, Vol. 2, Sep-Oct 1986, pp. 398-501.
4. Knoepfel, H., Pulsed High Magnetic Fields, North Holland (1970), p. 87.
5. Cobine, J.D., Gaseous Conductors, Dover (1958), p. 403.
6. Smith, D.L., Henderson, R.P., and Reinovsky, R.E., "Inductively Driven Imploding Plasma System for X-ray Generation," in Megagauss Physics and Technology, P.J. Turchi, ed., Plenum (1980), p. 337-349.
7. Capitelli, M., Ficocelli, V.E., and Molinari, E., "Equilibrium Compositions and Thermodynamic Properties of Mixed Plasmas, II-Argon-Oxygen Plasmas at 10^{-2} -10 Atmospheres, between 2000 °K and 35,000 °K. Centro Studio per la Chimica dei Plasmi. Universita degli Studi-Bari (1970). Tables with partial pressure of oxygen to argon of 10^{-4} .
8. Kannappan, D., and Bose, T.K., "Transport Properties of a Two-Temperature Argon Plasma," Phys. Fluids, Vol. 20, No. 10 (1977) pp. 1668-1672.
9. A. Bruckner, private communication (1970).

VII. APPENDICES

APPENDIX I

DETAILS OF SPECTROSCOPIC ANALYSIS SYSTEM

APPENDIX I

Details of Spectroscopic Analysis System

To enable spectroscopic analysis of the entire flow field, a digital spectral and spatial data acquisition system has been developed in a cooperative effort with the AFOSR-sponsored MIT group under Prof. Martinez-Sanchez. The system is comprised of a 1.2 meter, f/11.5 spectrograph with an EG&G/PARC intensified optical multichannel analyzer (SIT camera). The spectral and spatial output from the camera is processed by an IBM System 9000 laboratory computer for immediate background subtraction and signal averaging. The digital spectral and spatial data acquisition system development consists of interfacing systems, characterization of SIT camera performance, relative spectral calibration, optical alignment with spatial calibration, development of gate operation capability and computer analysis of data with associated software development. Also, considerable effort was necessary to shield the SIT camera and associated electronics from electromagnetic noise generated by the arcjet power supply and connections. Many issues as to SIT system performance surfaced during system characterization and calibration. These include linearity of signal, spatial uniformity of responsivity, background noise due to internal electronics, shot noise due to spurious electrons from the photocathode, and edge of field effects that cause pincushion distortion at frame edges (straight lines are observed as curves). More detailed discussion of the digital spectral and spatial data acquisition system and analysis of data from large diameter, annular arcjets will be the subject of a master's thesis by Daniel Kilfoyle (to be reported separately under AFOSR-sponsorship).

The SIT camera has a detector array of 512 x 512 pixels (262k pixels) with spatial size of 25 microns and a dynamic range of 16k. The interfaced system had resolution less than expected due to signal blooming from pixel to pixel (thus decreasing the observed spatial resolution) and range less than expected due to camera electronics (e.g., A/D converters) and to

software capabilities. The detector system was therefore limited to 250 horizontal pixels (spectral data) and to 128 vertical pixels (spatial data) or 32k data points per frame. The detector showed excellent spatial uniformity of responsivity but limited range of signal linearity of 0 to 600 counts as shown in Figure I-1. The detector system relative spectral response was measured with a calibrated tungsten filament lamp. The lamp was mounted to include effects of the input optics, turning mirrors and attenuation due to the chamber window material. The resultant relative spectral response normalized to 1.0 at 700 nm is shown in Figure I-2.

For initial system characterization, collimating input optics with a magnification of 5:1 (5 cm at source) and 2 cm downstream of an arcjet were used. Figure I-3 shows raw data as collected by the SIT camera system with the centerline of an argon arcjet at row 38 (approximately 1/3 up from the bottom of the page). Each vertical pixel represents approximately 0.05 cm. This raw data set has been zero-corrected, which effectively removes background noise due to the SIT internal electronics. Shot noise that is random in time for each pixel produces a random signal fluctuation on the detector spatially but with spatial frequencies on the order of 0.33 to 0.5 cycles per pixel. Figure I-4 shows a horizontal scan of Figure I-3 of row 55 (approximately 0.85 cm from the experimental center line). Note that each frame can contain spatial intensity information of more than one plasma emission line, in this case emission from Ar II lines 460.956 nm, 458.90 nm and 457.935 nm.

Software has been developed for further data reduction and analysis. For spatial electron density measurements the line emission profiles is measured and for spatial electron temperature determination the relative line emissivity is measured. Plasma electron temperature will be determined by the Boltzmann plot technique in which relative intensities of several spectral lines are compared. Figure I-5 shows row 32 of an Ar I emission line that has been zero-corrected. A small buffer containing only the line spatial emission is made and integrated to yield a

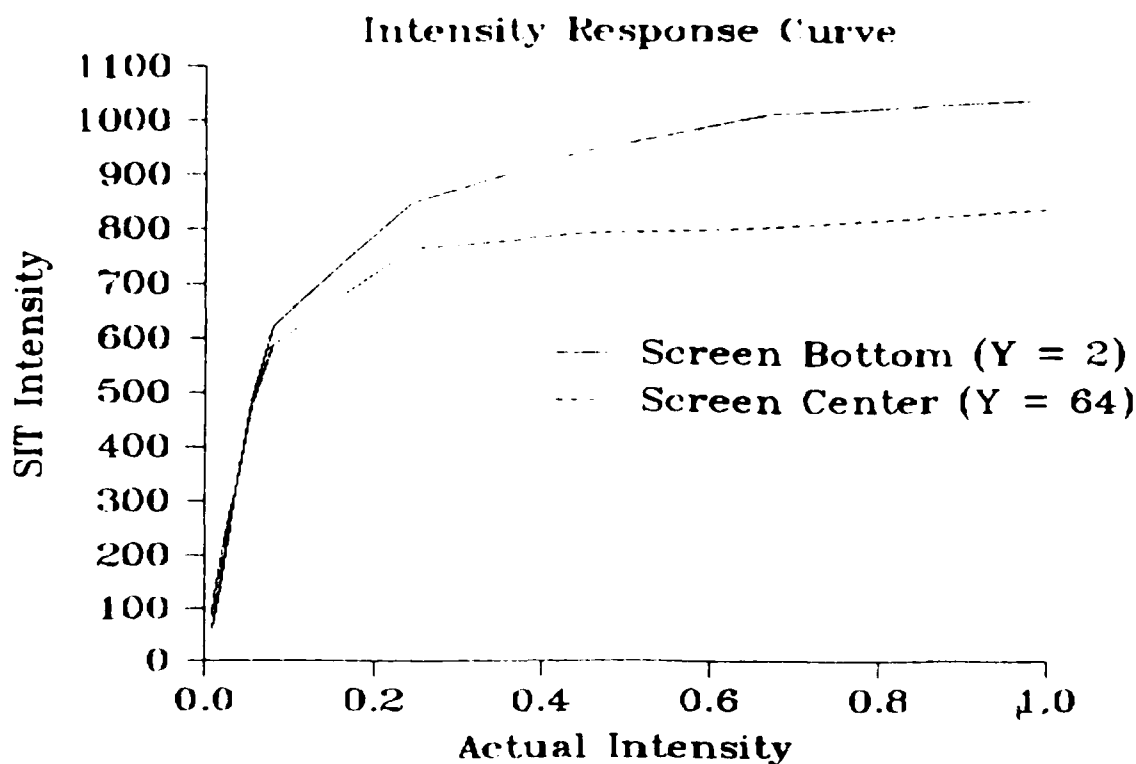


Figure I-1. SIT camera observed counts (vertical axis) vs relative input light flux (horizontal axis) at two horizontal rows shows good spatial uniformity of responsivity and linear response to 600 counts.

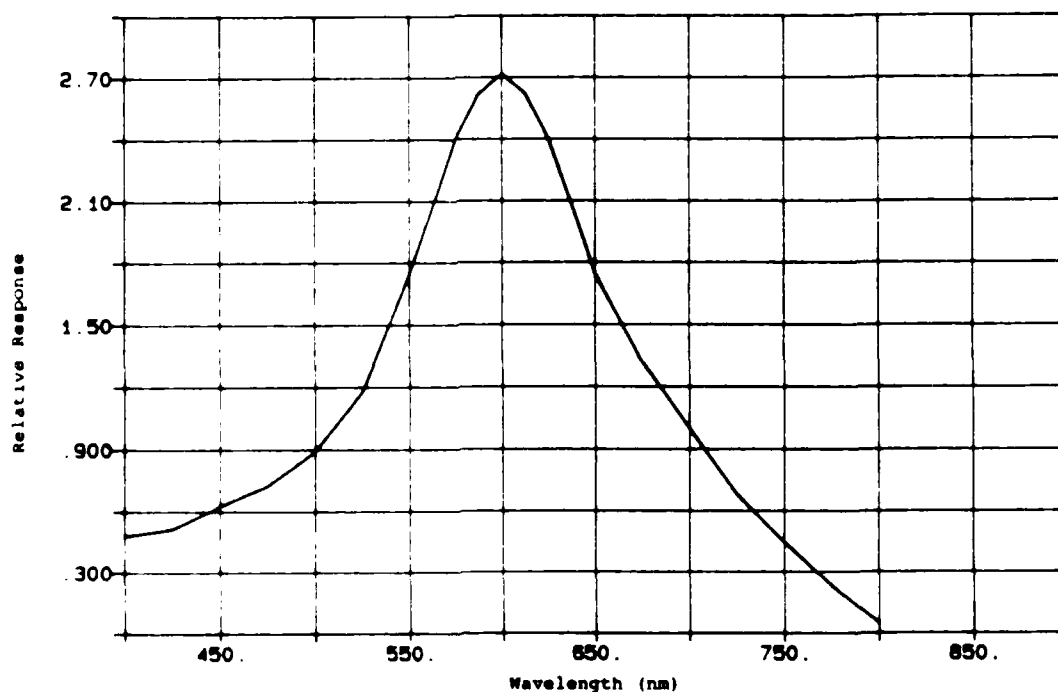


Figure I-2. Relative spectral system response normalized to 1.0 at 700 nm as measured by calibrated tungsten filament lamp between 400 and 800 nm.

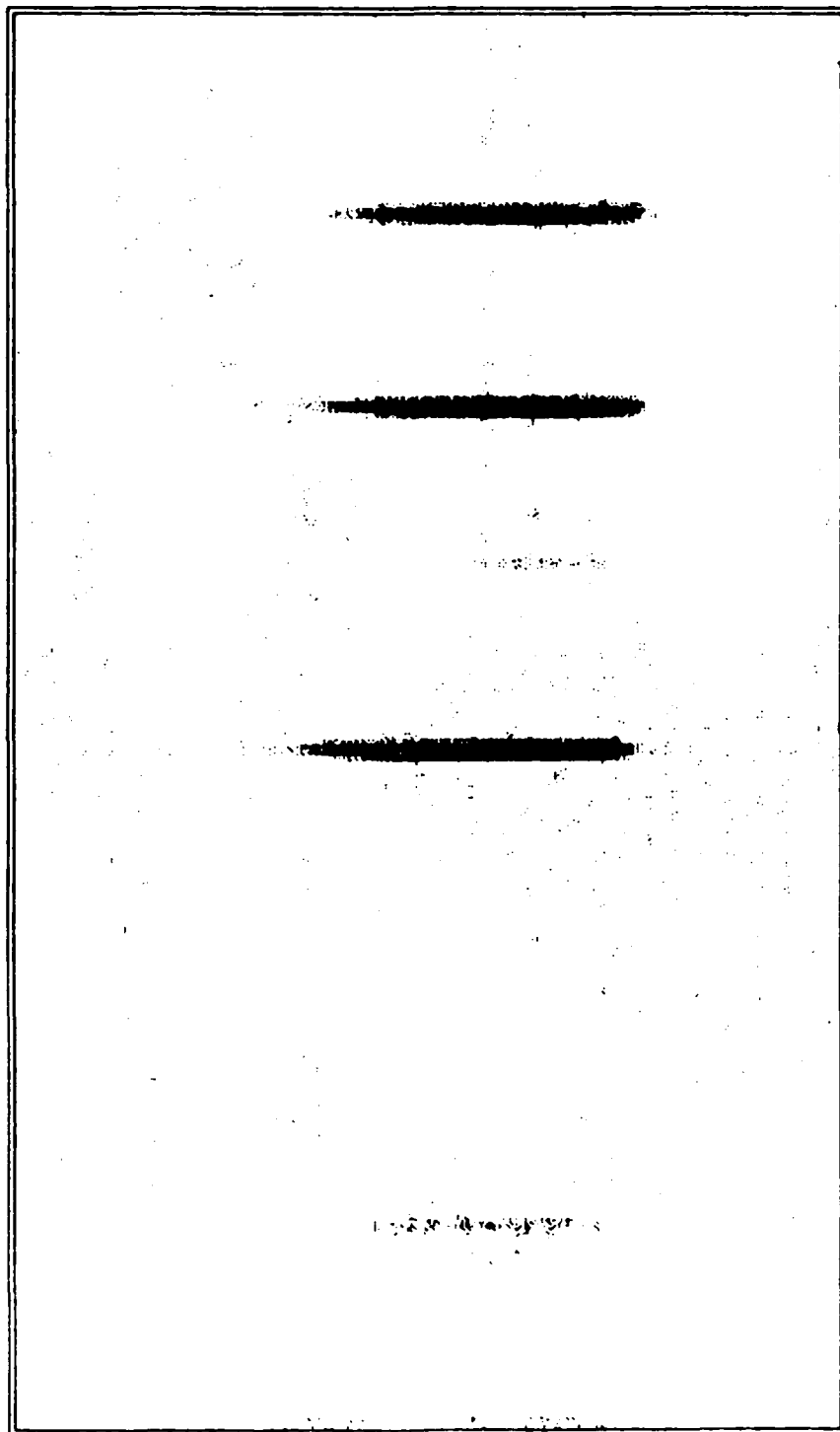


Figure I-3. Visual representation of SIT camera data of an argon arcjet. Each SIT camera data frame contains information in three dimensions: spectral, spatial, and intensity.

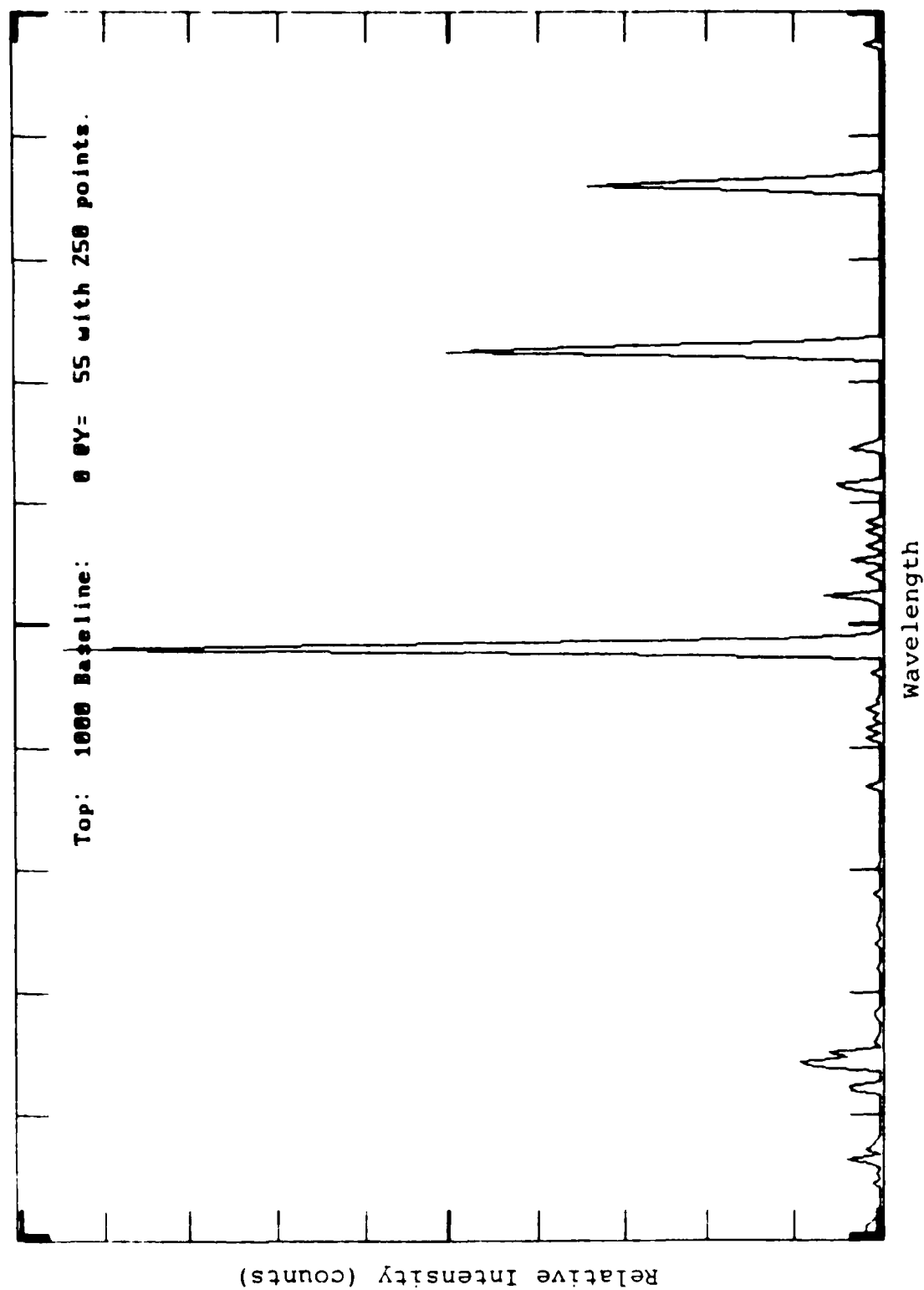


Figure I-4: Intensity vs wavelength of Figure I-3 at row 55 (approximately 0.85 cm from arcjet centerline) shows emission from argon ions at 460.956 nm (center), 457.90 nm (center right) and 457.935 nm (right).

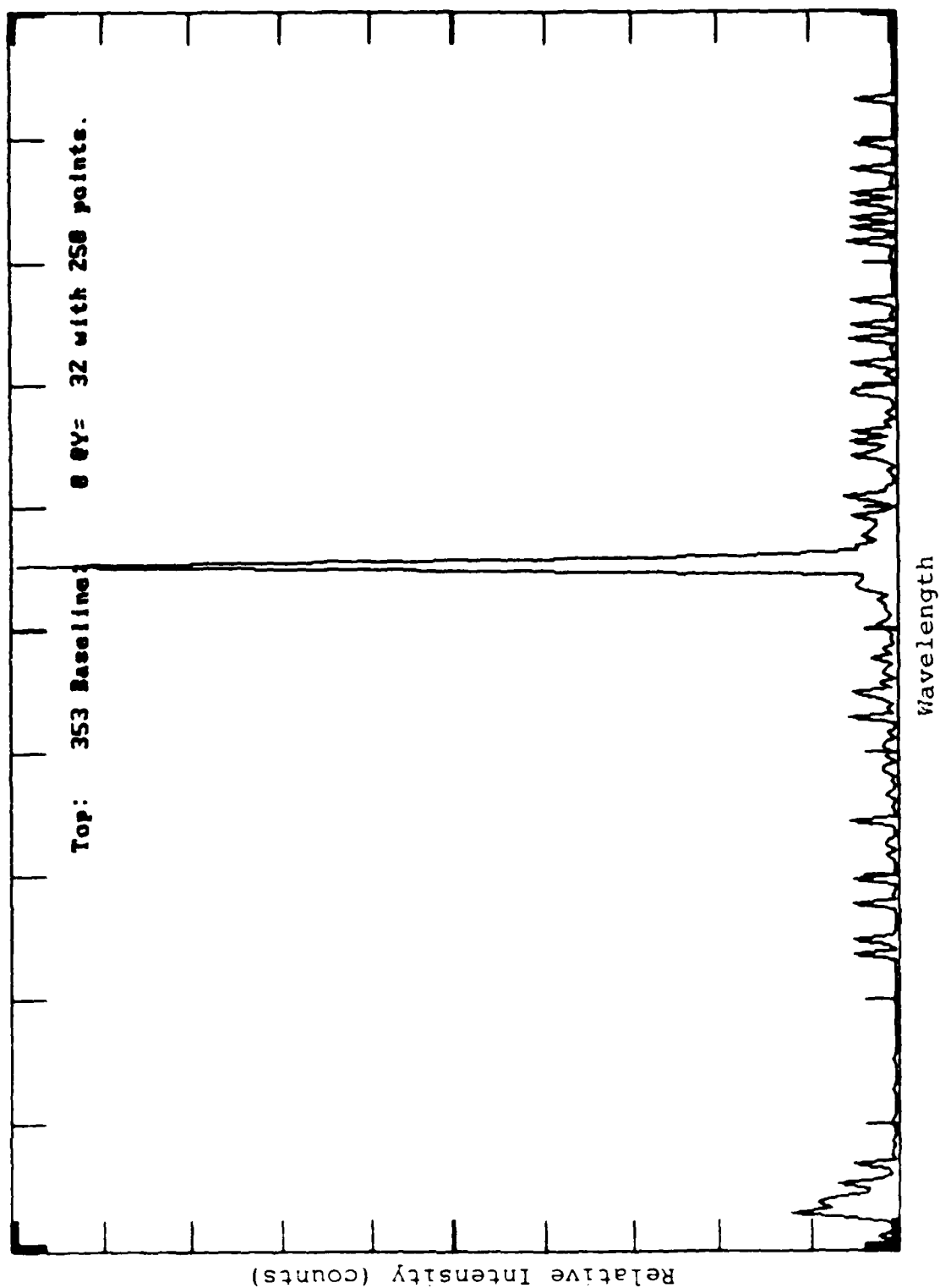


Figure I-5. Relative intensity vs wavelength of 727.293 nm neutral argon emission at 2 cm from exit plane of an argon arcjet.

raw intensity spatial profile shown in Figure I-6a. This data is then digitally-smoothed via a fast Fourier transform technique to eliminate higher spatial frequencies (shot noise) with result as shown in Figure I-6b. This smoothed raw intensity spatial profile is then Abel-inverted to yield spatially-resolved, spectral line emissivity that can be used for input to a Boltzmann plot routine to determine spatially-resolved electron temperature, as shown in Figure I-7.

Figures I-8 and I-9 show zero corrected data for 656.285 nm hydrogen emission 2 cm downstream of the arcjet with 1.6% hydrogen added to the argon in the plenum. For determination of electron density, the emission line profile and FWHM (full width at half maximum) must be measured. Software manipulation of emission line profile data is therefore performed both spatially and spectrally. Figures I-10a and I-10b show the hydrogen emission line at one radial position before and after smoothing. Figures I-11a and I-11b show unsmoothed and smoothed spatial emission profile along the hydrogen emission peak. The smoothed data is then Abel-inverted to yield true local line profiles. This information is first corrected by subtraction of line broadening due to temperature (Doppler broadening) and due to instrument broadening. The data is then fitted to a Lorentzian profile to yield spatially-resolved electron density.

Full flow-field visualization of many of the important parameters has been demonstrated with the new digital data acquisition system allowing more detailed and accurate data to be obtained in less time. Future system improvements are expected to increase sensitivity and dynamic range. In addition, software is being constantly upgraded for easier data reduction and presentation.

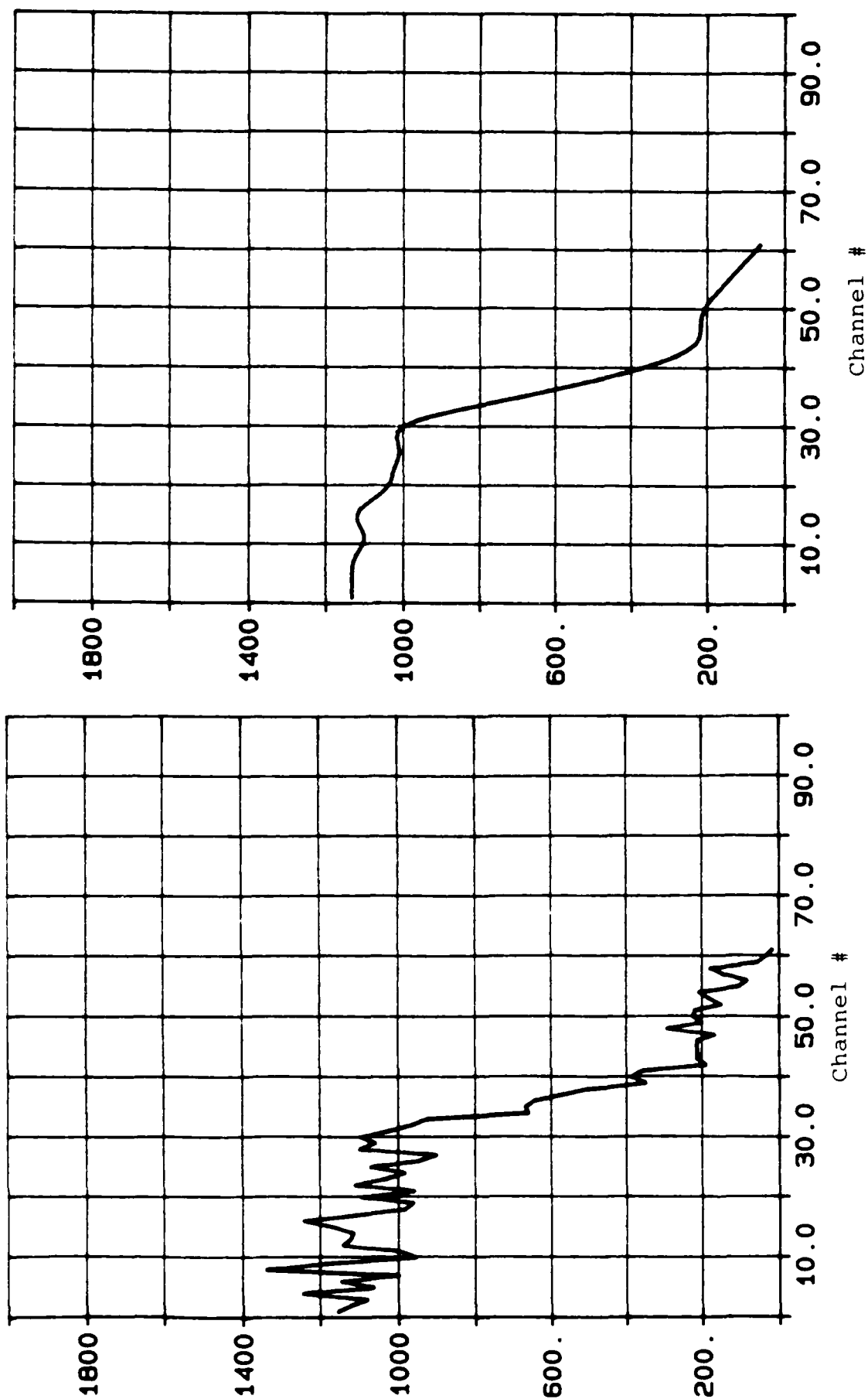


Figure I-6: Integrated spatial intensity profile of emission line shown in Figure I-5. (a) Raw intensity spatial profile; (b) Digitally-smoothed to remove high spatial frequencies characteristic of shot noise.

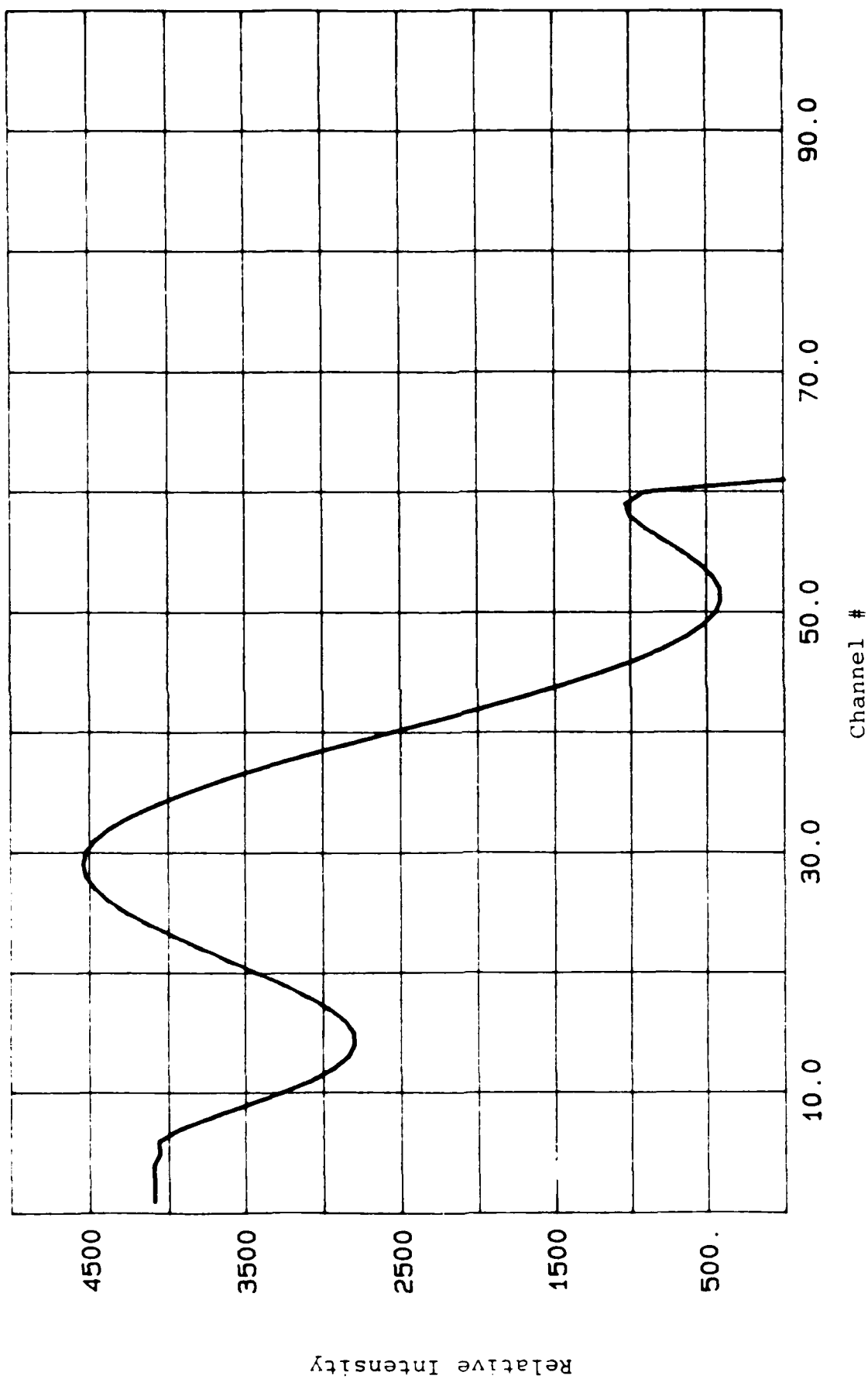


Figure I-7. Abel inversion of digitally-smoothed integrated argon emission shown in Figures I-5, I-6a and I-6b yield spatially-resolved spectral line emissivity.

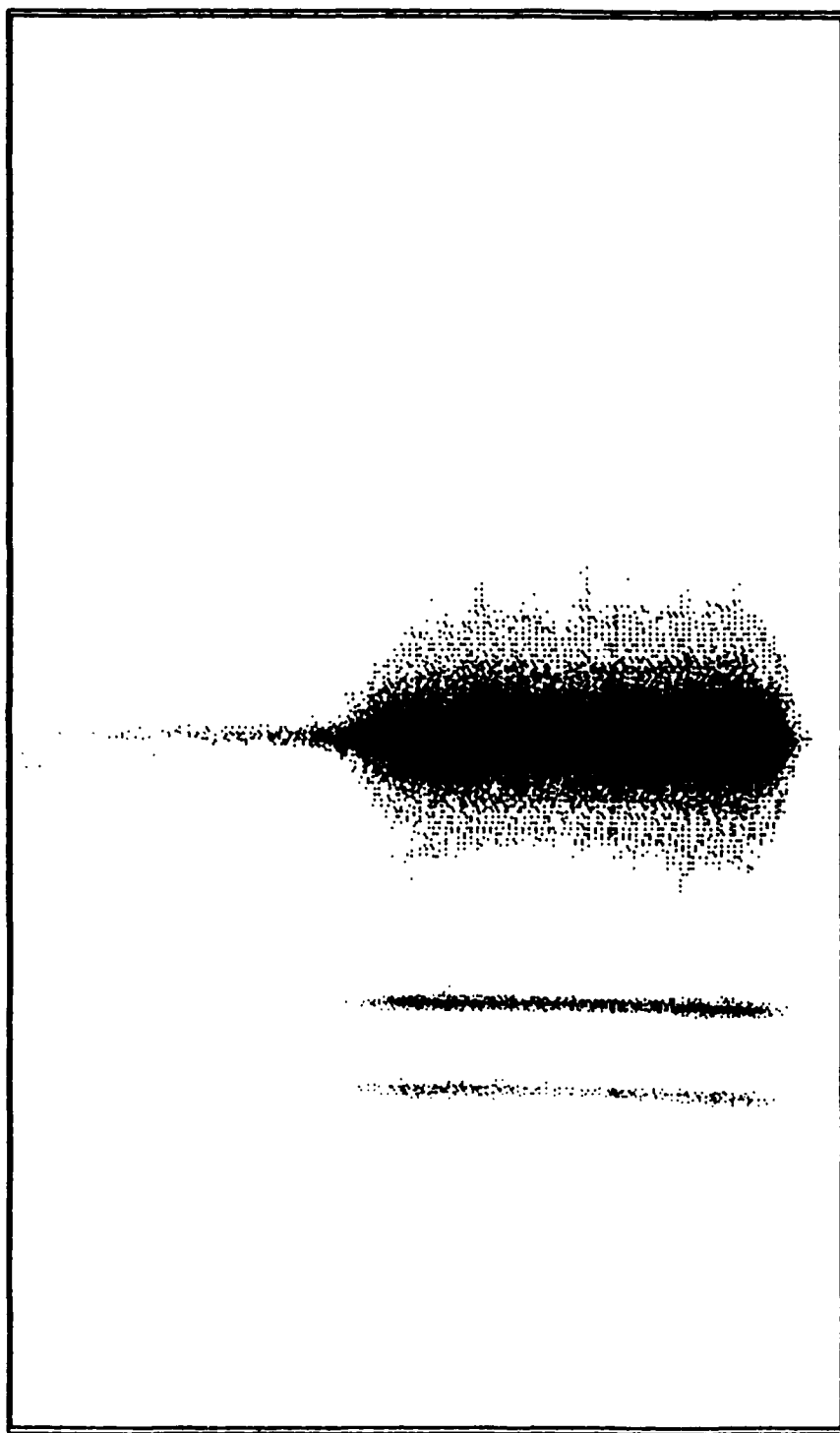


Figure I-8. Visual representation of 656.285 nm hydrogen emission 2 cm downstream of arcjet exit as observed by SIT camera system. Analysis of hydrogen spectral profile yields spatial electron density.

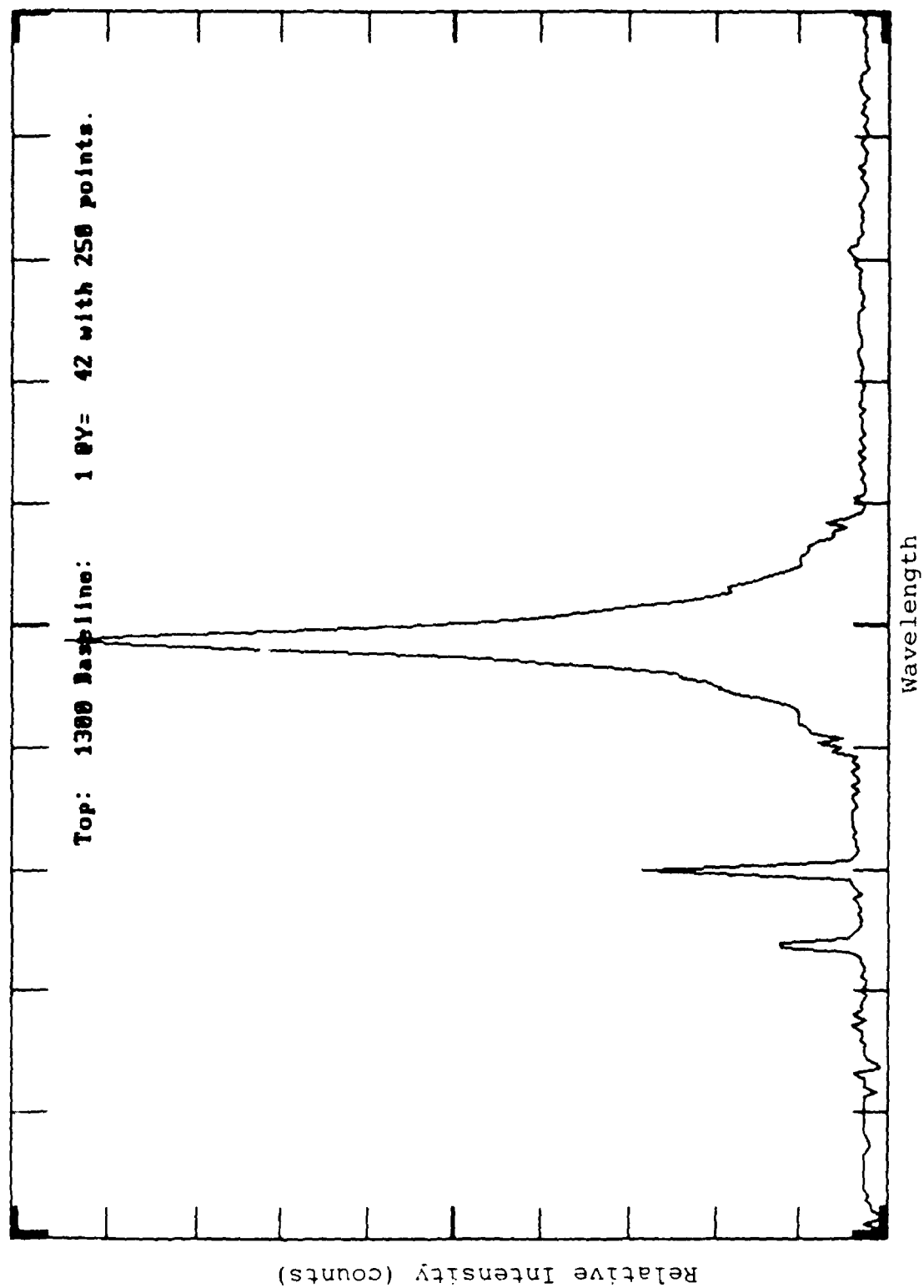


Figure I-9. Intensity vs wavelength of 656.285 nm hydrogen emission 2 cm downstream of arcjet exit at one spatial location.

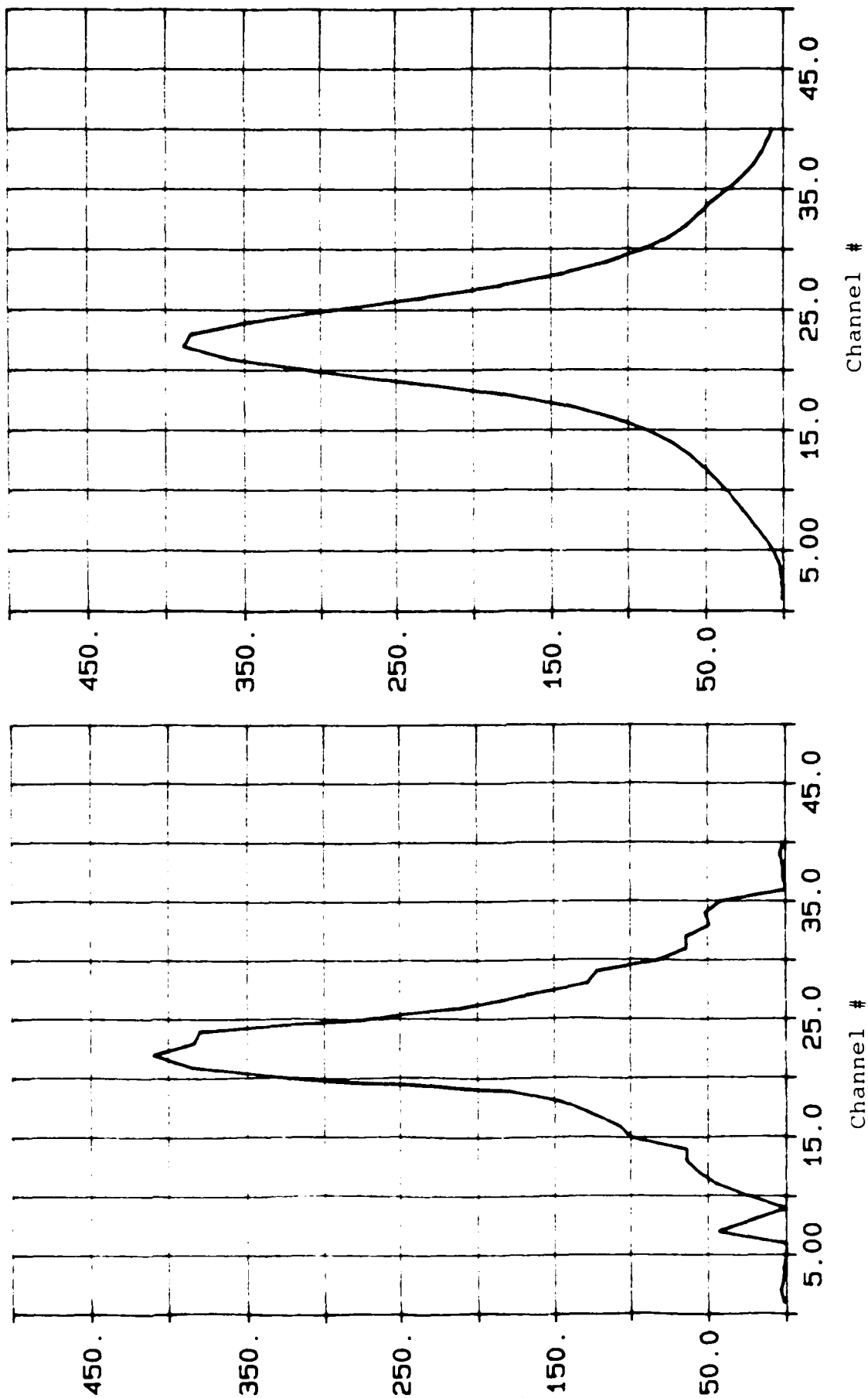


Figure I-10. Spectral emission line profile of 656.285 nm hydrogen emission from data at 2 cm downstream of an argon arcjet exit plane (1.6% hydrogen added to argon). (a) Raw data emission profile; (b) digitally-smoothed emission profile.

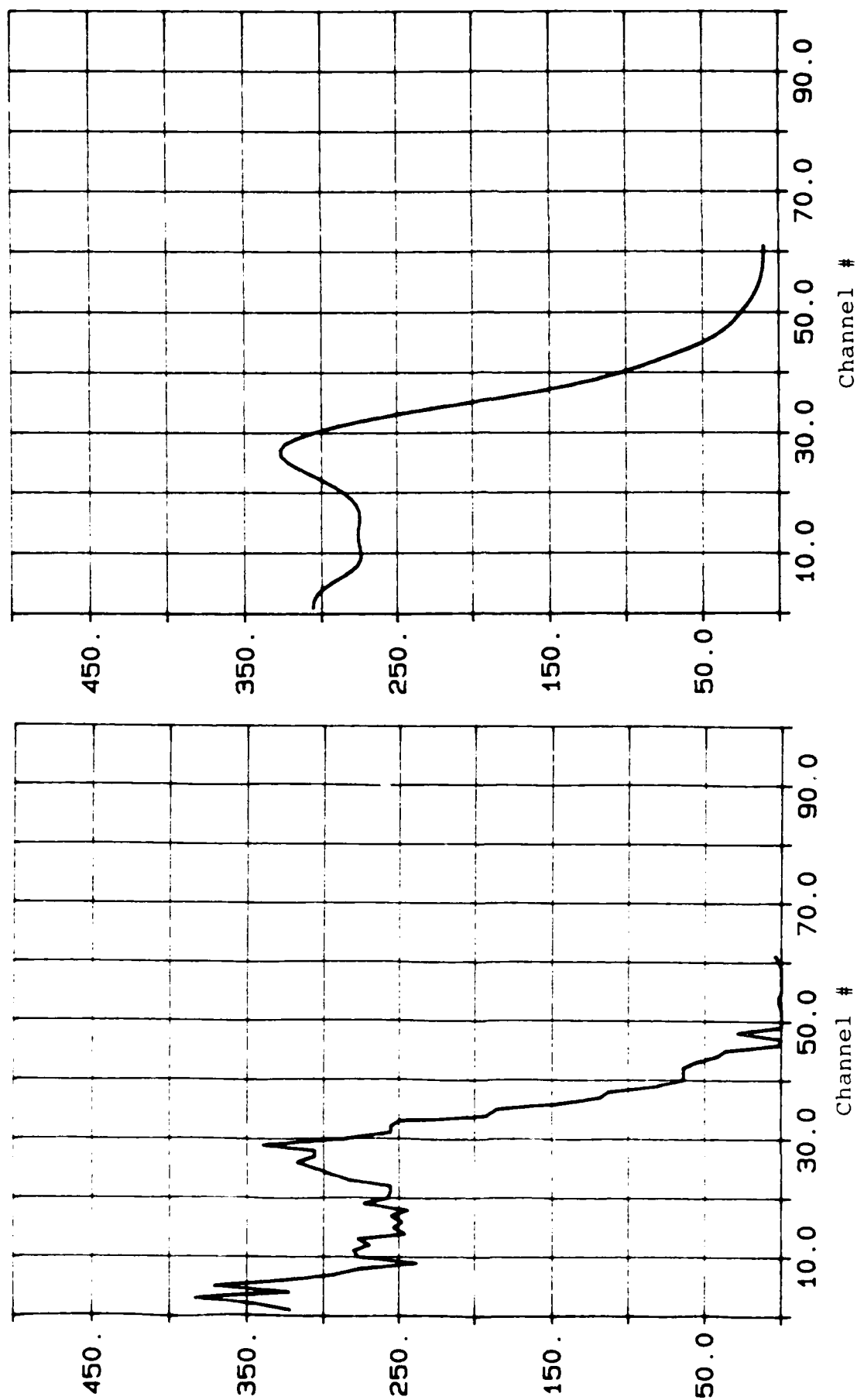


Figure I-11. Spatial emission profile along 656.285 nm hydrogen emission peak from data at 2 cm downstream of an argon arcjet exit plane (1.6% hydrogen added to argon). (a) Raw data spatial emission; (b) digitally smoothed spatial emission profile.

APPENDIX II

EFFECT OF AXIAL VARIATION OF ELECTRODE
SPACING ON MPD ARCJET BEHAVIOR

AIAA'87

AIAA-87-0998

**Effect of Axial Variation of Electrode
Spacing on MPD Arcjet Behavior**

D. J. Heimerdinger and M. Martinez-Sanchez,
Massachusetts Institute of Technology,
Cambridge, MA;

J. F. Davis and P. J. Turchi,
RDA Washington Research Lab,
Alexandria, VA

**AIAA/DGLR/JSASS 19th International
Electric Propulsion Conference**

May 11-13, 1987
Colorado Springs, Colorado

For permission to copy or republish, contact the American Institute of Aeronautics and Astronautics
1633 Broadway, New York, NY 10019

D. J. Heimerdinger and M. Martinez-Sanchez
 Massachusetts Institute of Technology
 Space Systems Laboratory
 Cambridge, Massachusetts 02139
 J. F. Davis and P. J. Turchi
 RDA Washington Research Laboratory
 Alexandria, VA 22314

Abstract

Two annular magnetoplasmadynamic (MPD) thrusters were constructed and operated in a regime where anode starvation processes limit the thrusters' performance. Magnetic field and floating potential measurements were conducted to determine the operational differences between a channel with constant interelectrode separation and a channel with an initial constant separation and a divergent exit. The channel with the constant electrode separation shows evidence of strong concentrations of current at both inlet and exit, along with strong indications of accompanying electrode erosion. In the divergent section, current densities were greatly diminished with decreased evidence of ablation. Evidence tends to indicate that electrode erosion is unavoidable for a starved anode; however, through spatial variation of the interelectrode spacing local ohmic heating can be controlled to minimize ablation of the other components, such as the cathode and backplate insulator.

Nomenclature

a	magnetoacoustic speed
B	magnetic induction field
E	electric field
F	thrust
J	total current
j	current density
m	mass flow rate
R	gas constant
r_a	anode radius
r_c	cathode radius
T	plasma temperature
\bar{u}	mean mass velocity
J	Hall parameter
γ	specific heat ratio
μ_0	permeability of free space
σ	plasma scalar conductivity

Introduction

The goal of the designer of an MPD arcjet is to obtain desirable overall performance. To achieve this goal, it is useful to manipulate internal distributions of current density and mass flow. In a previous paper, Martinez-Sanchez and Heimerdinger derived an approximate two-dimensional hydrodynamic MPD arcjet model which indicated that the performance and the internal distributions of the previously described

quantities can be manipulated by an axial variation of the interelectrode separation. This paper presents preliminary data from an experiment based on the analysis from reference 1.

MPD arcjets can be distinguished from other electric thrusters by their use of the $\mathbf{j} \times \mathbf{B}$ Lorentz force as their primary source of thrust. An approximate overall thrust equation shows this feature by the quadratic behavior of the thrust with the applied current and a weak dependence on geometry:

$$F = \frac{\mu_0 J^2}{4\pi} \left(\ln \frac{r_a}{r_c} + \frac{3}{4} \right)$$

For a given thruster geometry and mass flow rate, the efficiency also increases with current because of the transition from electrothermal acceleration due to the ohmic heating of the plasma to primarily an electromagnetic acceleration. Unfortunately, an operational limit called "onset" is reached where both erosion of the thruster and overall voltage have been noted to increase dramatically. The term onset originated from the appearance of megahertz terminal voltage oscillations which quickly grow in amplitude. Rudolph defined onset as that level where voltage oscillation reach 10% of the average terminal voltage.¹ In a given geometry, the onset limit scales approximately with the parameter J^2/m and thus correlates with the exhaust velocity.^{1,2}

In reference 1, the appearance of onset is attributed to an anode starvation phenomenon caused by axial deflection of the local current vector by the Hall effect. In figure 1, the Lorentz force, which is orthogonal both to the magnetic induction field and the current density vector, has a component directing the plasma towards the cathode. As the plasma adjacent to the anode becomes rarefied, deflection of the current vector is exacerbated as the Hall parameter grows due to the local decrease in collisionality. The region adjacent to the anode, increases in voltage to attract electrons and ensure current flow. Eventually the magnitude of this potential grows large enough for electrical breakdown to occur which allows concentrated arcs to form on the anode. This effect is intrinsic to MPD arcjet operation unless an external electric field is applied to halt the growth of axial current.

In addition to plasma depletion at the anode at high currents and low mass flow rates, the MPD arcjet can operate at a significant magnetic Reynolds number which implies a tendency towards convection of the magnetic field with the plasma.¹ Such convection tends to produce strong concentrations of current at the entrance and exit, due to the presence of a low back

This work was supported by the Air Force Office of Scientific Research under grant number AFOSR-86-0119D.

electromotive force (emf). From Ohm's law,

$$J + J \times B = \sigma(E + U \times B)$$

the plasma must take the entire electric field in the absence of back emf, thus forcing strong current concentrations to occur. Because of this, local heating of the insulator and electrodes occurs, accounting for their associated ablation.

The aim of this paper is to present data from an experiment based on a theory that claims the ability to control the distribution of the magnetic field, hence current density, in an MPD arcjet channel through careful axial variation of the interelectrode separation.

The Experimental Apparatus

A joint experiment between MIT and RDA Washington Research Laboratory in Alexandria, Virginia was conducted at the RDA facilities. A 400 kJ capacitor bank was modified into an eight stage LC ladder network to provide a flat quasi-steady current pulse to the MPD arcjet. The bank has a total capacitance of 2.0 mF where each section is separated by a 10 mH solenoid inductor. The pulse forming network PFN is designed with a high voltage ignitron switch at each stage so that the output waveform can be modified depending on the sequencing of ignitrons refer to figure 2. If a single ignitron ignitron #8 is fired, the resulting waveform has a duration of about 0.8 ms. This system requires a matched load of 0.2 Ω providing a maximum safe current pulse of 32 kA to the MPD arcjet. If ignitrons #1 and #8 are fired simultaneously, the impedance of the bank drops in half and a pulse of about 0.45 ms is achieved. With this configuration, a maximum safe current level of 65 kA can be supplied to the arcjet.

The PFN is connected to the arcjet, which is situated in a cylindrical stainless steel vacuum tank 6 m long and 0.6 m in diameter. The vacuum is maintained at a static level of $< 10^{-4}$ torr by two six inch diffusion pumps. The tank and associated pumps are electrically floating to prevent spurious alternate current paths for the PFN-arcjet circuit. The MPD arcjet assembly drawing in figure 3 shows the relation of its various components. The exterior of the arcjet is constructed as an anode sleeve which is isolated from the vacuum tank by a Plexiglas flange. The sleeve and the outer portion of the anode are hardcoat anodized with a 2 mil layer to inhibit current attachment beyond the anode lip. The cathode and mass injection assemblies both slide into the anode sleeve. A boron nitride insulator, seated in a Plexiglas assembly, isolates the anode from the cathode while a Mylar film and tape jacket surround the cathode sleeve completing the anode/cathode insulation. By constructing the feeds to the arcjet in this coaxial manner, the parasitic inductance of the device is kept to a minimum.

Mass is provided to the channel from a large reservoir placed close to the MPD arcjet channel. Six valves feed a preexpansion chamber directly upstream of 48 choked orifices. The gas flows through the choked orifices and expands through a boron nitride insulator, which also has 48 larger diameter holes, into the channel.

The anode is made of aluminum, primarily for its machinability, low weight, and low cost. The cathodes are made from copper primarily for its electrical properties, and it is both less

expensive and easier to machine into the required geometries than other more desirable materials.

A Tektronix data acquisition system is utilized for data collection, manipulation, and analysis. It is kept inside a large Faraday cage for shielding against stray electromagnetic noise. A block diagram of the MPD thruster system is seen in figure 4.

Initiation of the discharge occurs after the bank is charged to the appropriate operating value. At this point, the valves are opened with a 3 kV pulse and are held open until the required steady state mass flow rate is reached. After this delay (approximately 10 ms), the required ignitrons are triggered, several kilovolts appear across the electrode gap, breakdown ensues, and, after a short transient period (typically 150 μ s), quasi-steady operation is reached.

Thruster voltage is measured by a 1000:1 Tektronix voltage probe optically isolated from the data acquisition system. Floating potential is measured relative to the anode from a simple Langmuir probe through a 202:1 voltage divider. The floating potential probe is constructed primarily from a short piece of thin tungsten wire. The total current is measured by a large Rogowski loop surrounding the cathode sleeve at the base of the power connection. This probe measures the time rate of change of the enclosed magnetic flux, which is integrated to give the magnetic field, and, from Ampere's law, the total enclosed current. An active integrator with a 377 μ s integration time constant and a 70 ms associated droop time is used with this Rogowski loop. Enclosed current, at points inside the plasma, is measured from a small 10 turn Rogowski loop enclosed in a long Pyrex tube. Again, an active integrator with a 3.49 μ s integration time constant and a 70 ms associated droop time is used to integrate the time derivative of the magnetic induction field.

For this experiment, the bank was fired with #1 and #8 ignitrons so that an operating point of 60 kA at 4.0 g/s of Argon was obtained.

Two MPD arcjet channels were constructed and diagnosed. A constant area channel consists of a cylindrical anode and concentric cathode with a constant interelectrode separation of 1.8 cm. A second channel, the modified flared channel, was based on a calculation from the theory in reference 1 for uniform current density distributions along the electrodes. To minimize cylindrical effects, the annular channel geometry was based on a large cathode diameter compared to the interelectrode gap. For a mass flow rate of 4.0 g/s of Argon at an operating point of about 60 kA, a channel with the area variation shown in figure 5 is predicted by the theory. In order to examine the behavior of the two channels, we chose to operate in the vicinity of onset, where onset is predicted by the theory as the solution where zero density is encountered somewhere along the anode. The design theory, for which this calculation is based, neglects the initial ionization processes that occur in a region of the discharge dominated by ohmic heating where large changes in plasma velocity and density occur. For this reason, a low speed near the entrance for a given mass flow rate leads to large variations in the interelectrode separation. This is immediately seen in figure 5 at the channel entrance upstream from the point of minimum area. However, for this experiment, in order to ensure reliable ignition at the inlet, only the portion

downstream from the point of minimum area was flared. The upstream portion remains fixed at 1.8 cm. Hence this device is called the modified flared channel. In both geometries, the anode remains the same and all channel variation is taken by the cathode. This is done for simplicity in the machining of the electrodes.

Results and Discussion

Both channels were probed to determine current and floating potential distributions. Typical probe responses are seen in figures 6 and 7. The enclosed current and floating potential contours for the two channels are found in figures 8 and 9 respectively. Determination of the plasma potential from floating potential measurements necessitates knowledge of the electron temperature and ionic species.⁷ Other work has shown that this temperature variation is small so that the differences in floating potential is sufficient for the calculation of electric fields.

In both channels, large axial currents are found in the anode region. This implies large local values of the Hall parameter. From the floating potential contours, there also appears to be a large positive potential drop at both anodes. A large Hall parameter implies a deficiency of charge carriers which correlates with the large positive anode fall required to pass all of the current. Based on reference 1, it is apparent that both channels are operating beyond the onset level.

Typical terminal voltage traces do not display the high frequency oscillations that typically characterize onset. Megahertz voltage oscillations are seen, however, in the floating potential characteristics. Terminal voltage scaling shown in figure 10 does not display the cubic dependence of voltage that one would expect to precede onset.¹⁻⁴

Turchi suggests that an increase in ablation as the exhaust speed exceeds the Alfvén critical speed, based on ablation energy, may preclude a cubic dependence of voltage on current in MPD arcjet operation, even if the dominant acceleration mechanism is electromagnetic.⁹

Examination of both thrusters shows strong evidence of ablation. Both anodes show erosion primarily at their exit lip. Both cathodes also show erosion, especially in the entrance region. In fact, after less than 100 discharges, copper from the cathode is plated on the boron nitride insulating injector plate. The anode wear is similar in both geometries, however, the cathode wear is markedly different. For the constant area channel, bands about a half a centimeter wide are seen at both the entrance and the exit. The band at the entrance looks like freshly machined copper, indicative of strong and even erosion. The band at the exit is well defined but is not quite as clean as the one at the entrance. The band at the entrance are largely composed of semicircular clean regions adjacent to the mass injection sites. More clean spots are noted about a half to one centimeter further downstream directly in line with the mass injection holes in the boron nitride insulator. The remaining cathode shows strong evidence of fine line arc structures extending from the cathode downstream and almost to the cathode root. These fine structures are branch-like and tend to branch in an upstream direction.

In the modified flared channel, the clean

band at the exit is absent, but there is a wide clean band at the entrance between 0.75 cm to 1.3 cm in extent. Unlike the other bands, this one has a very poorly defined downstream edge. The fine line structures are completely absent on this cathode. Drawings of both cathodes are found in figures 11 and 12.

Figure 13 shows a graph of the current density along both cathode surfaces. In both cases, strong concentrations are found in the initial portion of the channel. In the constant area channel, the current density drops to a low value at mid-channel and then increases dramatically near the exit. The current density in the modified flared channel remains high until just before the beginning of the flared region where it subsequently drops significantly below the level found in the constant area channel.

The theory tends to support the trends seen in figure 13. At the channel entrance, the plasma is moving slowly so the back emf is low. In both channels, the interelectrode distance at the entrance is the same, and both plasmas must take the total electric field in the absence of any significant back emf. At the exits the magnetic field drops towards zero and once again the back emf is small. In this region, the plasma once again must take the total electric field; however, in the modified flared channel, the local electric field decreases due to the increased interelectrode separation, so a strong current concentration is mitigated. Since the current density is lower in the flared region, and the same current is passed as in the constant area channel, the current density in the upstream portion of the modified flared channel must increase. This may account for higher ohmic heating which may lead to an elevated plasma temperature, and therefore higher ionization fraction and electrical conductivity, in the modified flared channel.

The theory also indicates that high magnetic Reynolds number flows in constant area channels tend to have strong current concentrations at the exit as the magnetic field goes to zero. Also it shows that the magnetic field in a flared channel is more evenly distributed due to the controlled plasma expansion and the convection of the magnetic field with the fluid at higher magnetic Reynolds numbers. In this operating regime, the magnetized plasma behaves analogously to an ordinary compressible gas except that the speed of sound is replaced by the magnetoacoustic speed, defined as

$$a = (\gamma RT + \frac{B^2}{2\mu_0})^{1/2}$$

which is a combination of the speed of sound and the Alfvén speed.

Data for the constant area channel does not seem to exhibit this behavior. The theory neglects the effect of viscosity which may account for some of the differences. In this channel, the presence of a large axial component of the current acts to deplete the anode and pressurizes the cathode. The moving plasma, blocked by the cathode must move along it, which may be sufficient for viscous dissipation to slow the plasma. If the plasma speed is sufficiently lowered, the corresponding magnetic Reynolds number for the arcjet may be low enough for a more uniform axial decrease of magnetic field. If the magnetic field is sufficiently low at the exit,

ordinary gas dynamic choking can occur (as in the case of ordinary gas dynamics with Fanno flow for flows with friction and Rayleigh flow for flows with heating), thus limiting the effective exhaust velocity to that corresponding to Mach 1.

However, the modified flared channel does exhibit some of the trends anticipated by the theory. Although pressurization of the cathode is evidenced by the current contours, the flaring of the cathode tends to reduce the obstruction of the plasma motion. Also, an increased plasma temperature can lead to a strong drop in plasma viscosity as shown in figure 14.¹² This could act to sufficiently lower the viscous losses expected in this region. Therefore, the magnetic Reynolds number may not be reduced significantly; in fact, the thermodynamic expansion encountered in the nozzle region would allow for an increase in the plasma velocity beyond the appropriate sonic or magnetoacoustic speed, which would translate to an increase in the magnetic Reynolds number.

This is further evidenced by the difference in the terminal voltages measured in the arcjets. Martinez-Sanchez shows that the terminal voltage decreases with increasing magnetic Reynolds number.⁶ In this experiment, the constant area channel is seen to operate at a mean voltage of 78.1 ± 1.6 volts, while the modified flared channel operates at 70.0 ± 1.8 volts.

The plasma discharge near the anode appears quite different from the cathode. The anode current densities and voltage drops are plotted in figure 15. Both geometries exhibit large potential drops indicative of starved anodes. For the most part, the magnitude of the voltage drop follows the magnitude of the current density. The only place where there is a deviation from this behavior is at the entrance to the modified flared channel. Here, high current density is associated with a low voltage drop. This tends to suggest the development of concentrated arcs, substantiated through examination of the anode.

In this initial region, there is a high demand to pass current due to the low back emf, but the gas has a low conductivity since it has not yet become fully ionized. The local electric fields may not yet be sufficient to support a diffuse discharge so the plasma may have no other choice but to arc strongly and locally heat the plasma. As the plasma is convected downstream, its conductivity increases, and the arc may become more diffuse. Eventually, no severe arcing is necessary, as the conductivity and the back emf have risen to a level so that a more diffuse discharge may be supported. This is evidenced by the wear pattern on the inside of the anode. Arcing, adjacent to the injectors at the anode, is seen with tracks that appear to continue downstream. As the arcs continue downstream, they appear to broaden and weaken until the wear on the anode surface becomes more azimuthally uniform; this occurs about a third of the way down the anode from the channel entrance.

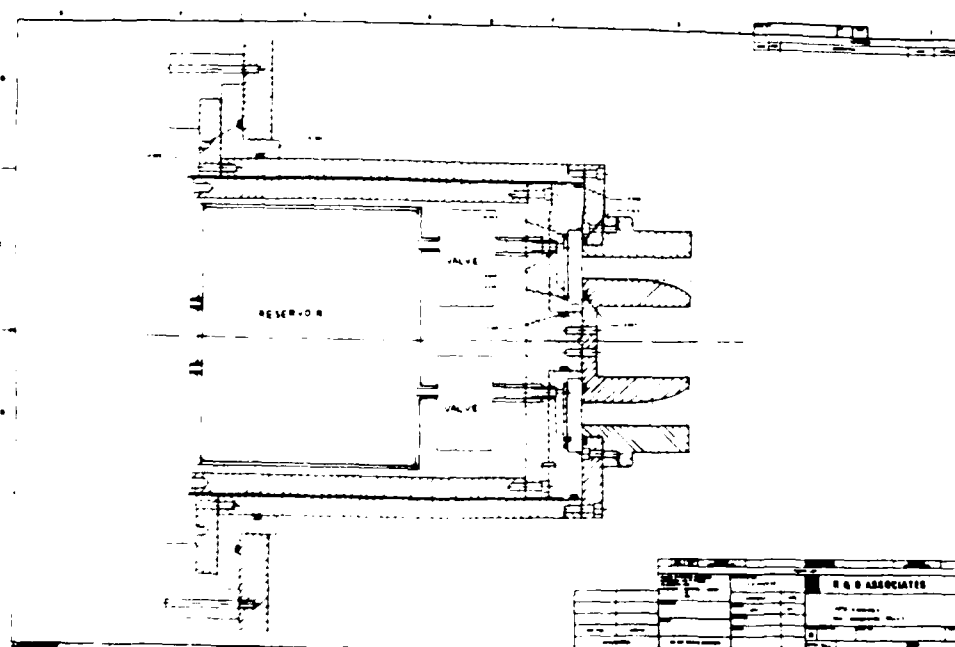
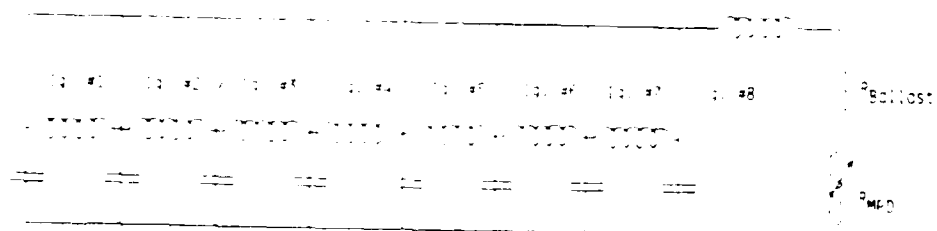
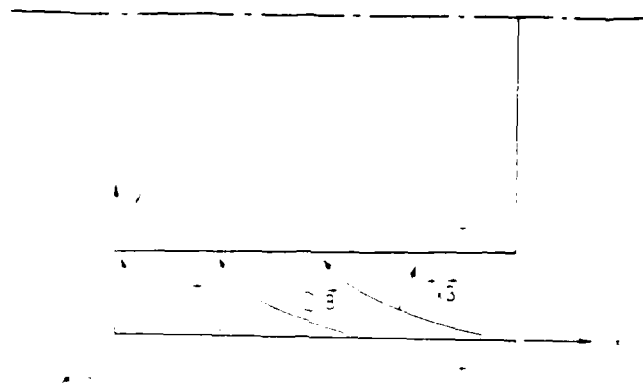
Significant erosion can occur in other areas of the MPD arcjet for reasons that are not necessarily associated with anode current conduction onset. In this experiment, erosion of the cathode has been locally decreased by flaring the cathode. Theory suggests that this is also valid for the entrance region.² By decreasing the local electric field, the current is spread out, thereby decreasing its density and the associated local ohmic heating. This not only protects the cathode, but the insulator region as well.

Conclusion

Preliminary examination of data from an MPD arcjet experiment has shown that arcjet operation can be modified through a variation of the interelectrode separation. Further experimentation should be done to study the effect of increasing the interelectrode distance at the entrance in a similar manner as was done at the exit to alleviate the high concentration of current along the cathode. If the expected decrease in current density is encountered, additional experimentation using better cathode materials with superior ablation properties such as thoriated tungsten or barium oxide impregnated tungsten¹³ should be done, as well as continued study of the MPD arcjet plasma properties so as to understand loss mechanisms such as friction in the MPD arcjet. And finally, additional experimentation should be conducted to study the thruster operation below onset.

References

1. Martinez-Sanchez, M. and Heimerdinger, D.D., "Two-Dimensional Analysis of an MPD Arcjet," AIAA-85-2040 presented at the AIAA/DGLR/JSASS 18th International Electric Propulsion Conference, Sept. 30 - Oct. 2, 1985, Alexandria, VA.
2. Jahn, R.G., Physics of Electric Propulsion, McGraw Hill Book Company, New York, 1968.
3. Rudolph, L.K., and Jahn, R.G., "The MPD Thruster Onset Current Performance Limitation," Ph.D. Dissertation, Princeton University, Princeton, NJ, MAE Report No. 1491, September 1980.
4. King, D. Q., Smith, W. W., Jahn, R.G., and Clark, K. E., "Effect of Thrust Chamber Configuration on MPD Arcjet Performance," Proceedings of the Princeton/AIAA/DGLR 14th International Electric Propulsion Conference.
5. Malliaris, A. C., John, R. R., Garrison, R. L., and Libby, D. R., "Performance of Quasi-Steady MPD Thrusters at High Powers," AIAA Journal, Vol. 10, No. 2, February 1972.
6. Martinez-Sanchez, M., "The Structure of Self-Field Accelerated Plasma Flows," AIAA-87-1065 presented at the 19th AIAA/DGLR/JSASS International Electric Propulsion Conference, May 11-13, 1987, Colorado Springs, CO.
7. Huddleston, R. H. and Leonard, S. L., Plasma Diagnostic Techniques, Academic Press, New York City, 1965.
8. Ho, D. D., Jahn, R. G., "Erosion Studies in an MPD Thruster," Masters Thesis, Princeton University, Princeton, NJ, MAE Report No. 1515, May 1981.
9. Turchi, P. J., "Critical Speed and Voltage-Current Characteristics in Self-Field Plasma Thrusters," Journal of Propulsion and Power, Vol. 2, Sept.-Oct. 1986, pp. 398-401.
10. Hirsch, M. N. and Oskam, H. J., ed., Gaseous Electronics, Volume 1: Electrical Discharges, Academic Press, New York City, 1978.
11. Uematsu, K., Mori, K., Kuninaka, H., and Kuriki, K., "Effect of Electrode Configuration on MPD Arcjet Performance," Paper IEPC 84-11 presented at the 17th AIAA/DGLR/JSASS International Electric Propulsion Conference, Tokyo, Japan, 1984.



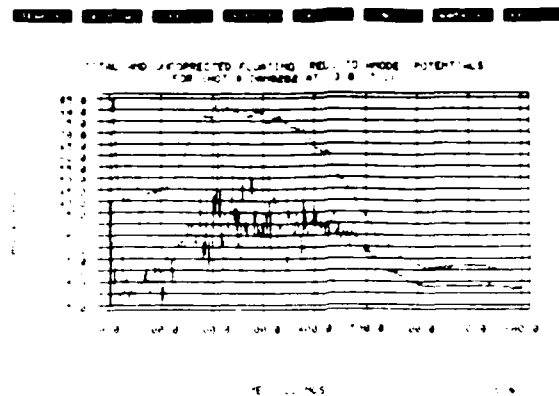
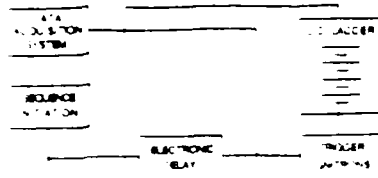


Figure 7. Typical, Total, and Floating Potential, Probe (Oscilloscope Trace)

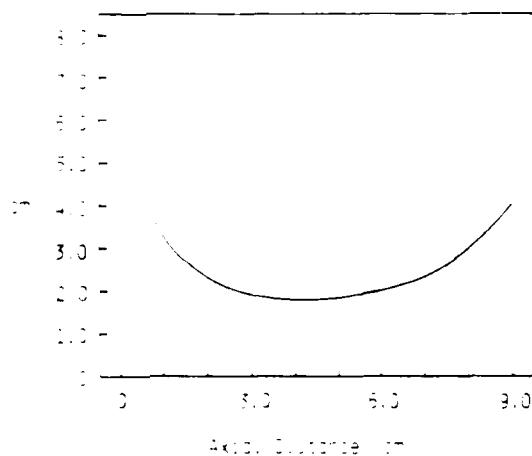


Figure 8. Calculated Interelectrode Separation for $j = 40 \text{ kA/m}^2$, $m = 4.0 \text{ s/s}$

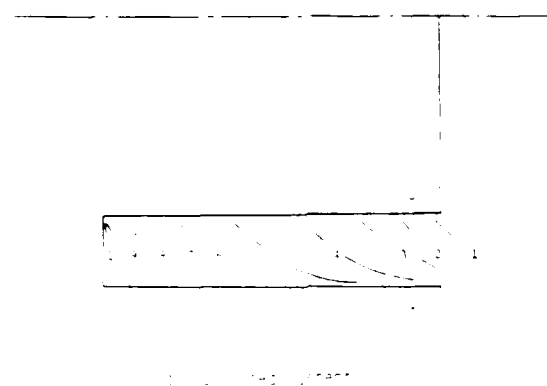


Figure 9. Enclosed Current

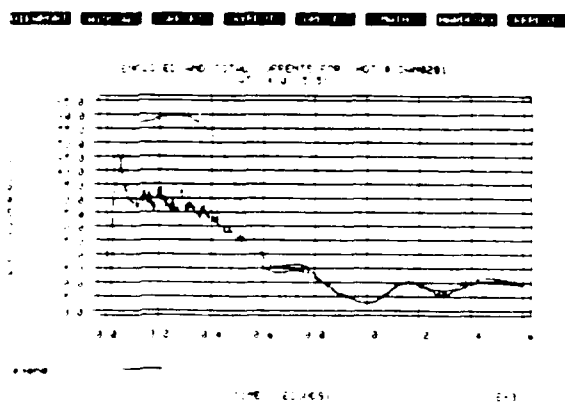


Figure 10. Typical Enclosed and Total Current Oscilloscope Trace

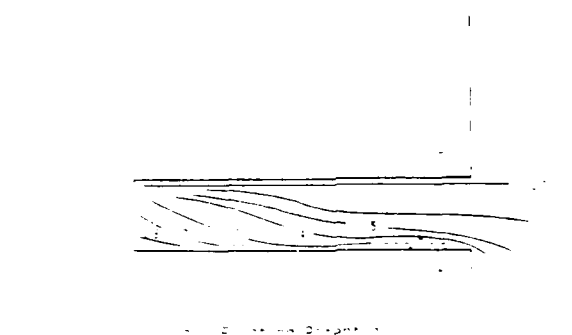


Figure 11. Floating Potential, Contours in the Constant Area Channel

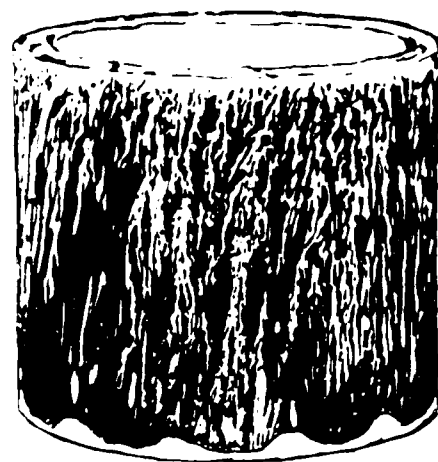
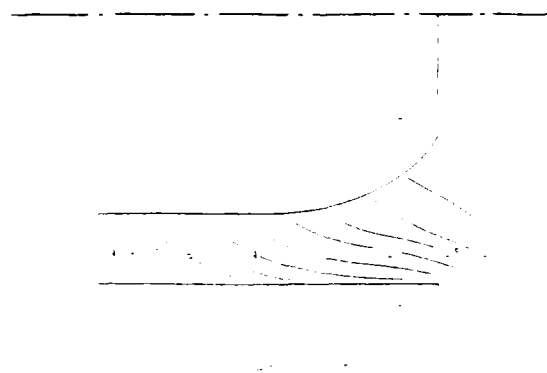


Figure 11 Sketch of the Constant Area Cathode After Multiple Firings

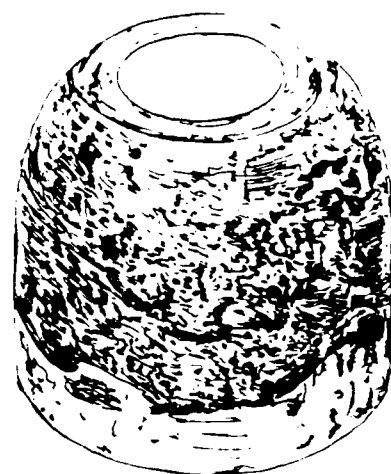
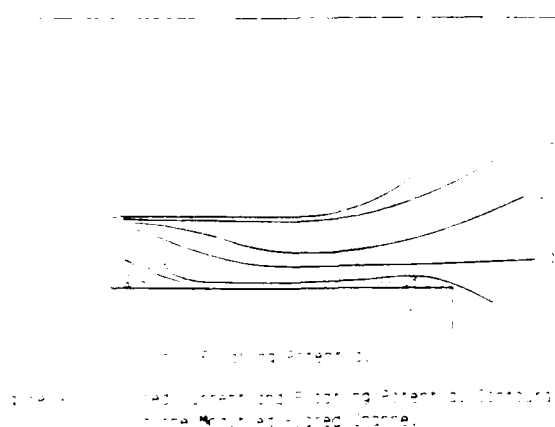


Figure 12 Sketch of the Modified Flared Cathode After Multiple Firings

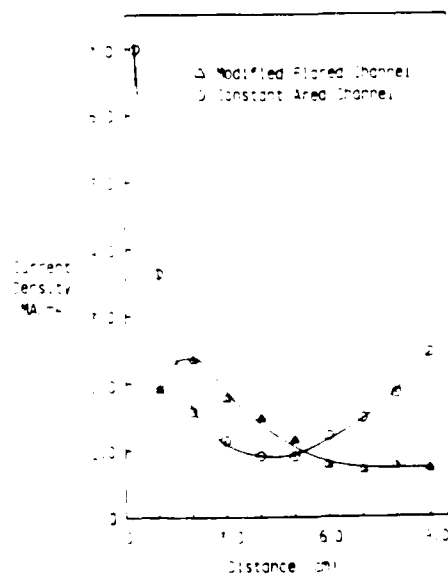
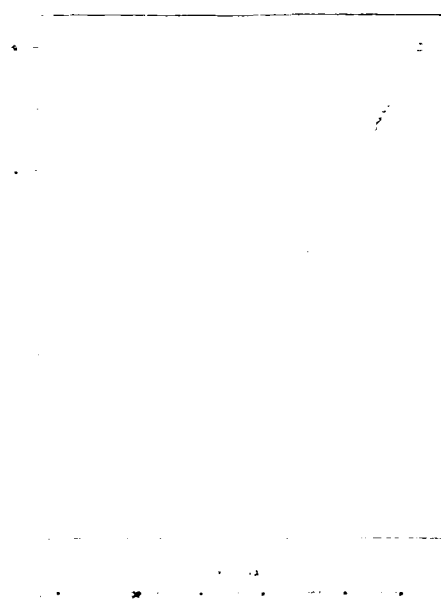


Figure 13 Cathode Current Density Distributions

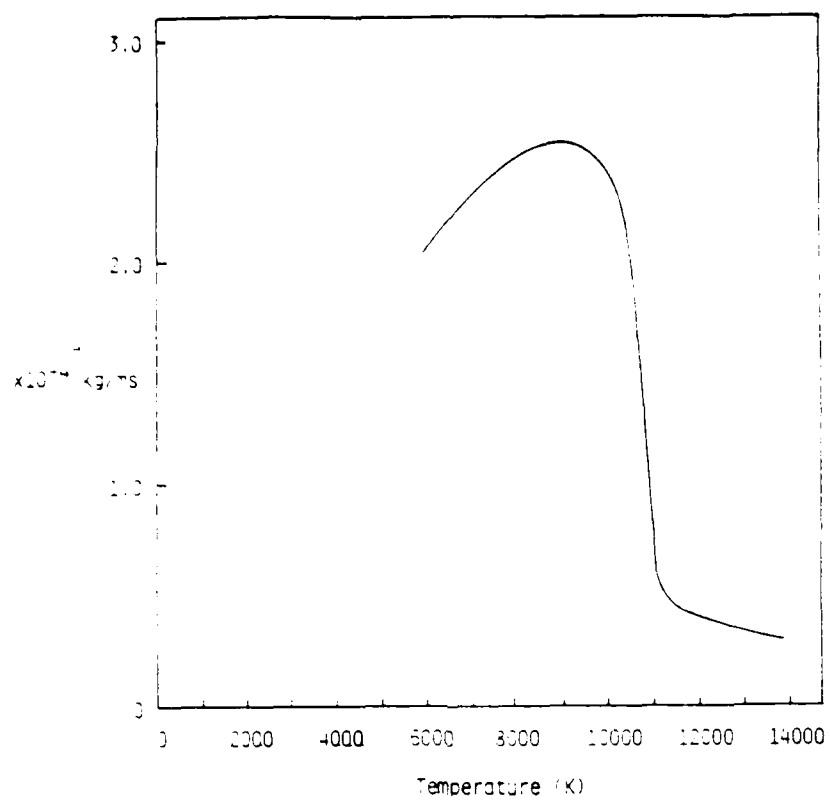


Figure 14: Viscosity of an Equilibrium Argon Plasma at 0.01 atm.

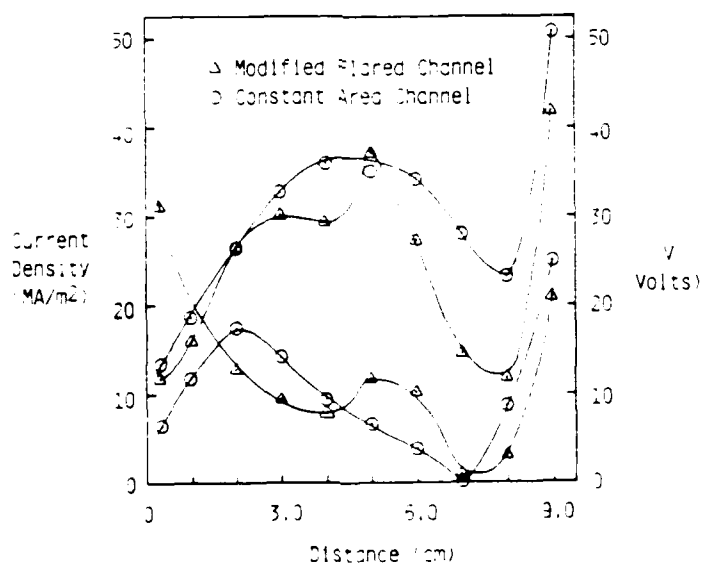


Figure 15: Distributions of Voltage Drops and Current Densities in Anode Vicinity

APPENDIX III

CRITICAL SPEED AND VOLTAGE-CURRENT
CHARACTERISTICS IN SELF-FIELD PLASMA THRUSTERS

Critical Speed and Voltage-Current Characteristics in Self-Field Plasma Thrusters

P. J. Turchi



Volume 2, Number 5, September-October 1986, Page 398

AMERICAN INSTITUTE OF AERONAUTICS AND ASTRONAUTICS • 1833 BROADWAY • NEW YORK, N. Y. 10019

Critical Speed and Voltage-Current Characteristics in Self-Field Plasma Thrusters

P. J. Turchi*

RDA Washington Research Laboratory, Alexandria, Virginia

To examine possible exhaust velocity limitations in high power magnetoplasmadynamic (MPD) arcjets, a power balance model is constructed. A special feature of this model is that the discharge thickness is inversely proportional to the velocity of the high-speed electrically conducting flow created by the discharge and its self magnetic field. Resistive dissipation then scales with electromagnetic thrust and flow speed. Ablation of arcjet materials adds to the total mass flow when the input propellant flow is insufficient to carry away the dissipated power. At high power levels, the exhaust velocity may plateau because of such mass addition at values comparable to Alfvén critical speed. At lower powers, incomplete ionization and coupling of the injected neutral flow in the discharge can also result in such a velocity plateau (as interpreted by voltage and plume measurements). The voltage-current characteristics of MPD arcjets are discussed and research directions are indicated.

Nomenclature

B	= magnetic (induction) field
E	= first ionization level of propellant atom
g	= geometric factor relating discharge volume to thruster area
j	= current density
J	= total current
J_{crit}	= total current for which $\beta = 1$
m	= mass of propellant atom
\dot{m}	= total mass flow rate
\dot{m}_a/\dot{m}_f	= mass flow rate of ablated material and propellant material, respectively
Q_a	= heat absorbed per unit mass of ablated material
Q_f	= heat absorbed per unit mass of propellant material
r	= characteristic radius of thrust chamber
r_o/r_i	= ratio of outer-to-inner current attachment radii
Re_u	= magnetic Reynolds number
u	= exhaust speed
u_{crit}	= Alfvén critical speed
u_c	= characteristic speed (for $\beta = 1$)
u_a	= exhaust speed of ablation thruster ($\dot{m}_f = 0$)
u_e	= speed of electrically conducting portion of flow
u_p	= electron flow velocity
u_i	= ideal exhaust speed (full coupling, no ablation)
V	= voltage
ρ	= mass density
σ	= electrical conductivity
μ	= magnetic permeability
δ	= characteristic discharge thickness
δ_a	= characteristic discharge thickness for ablation arc
ν	= characteristic volume of discharge
Ω	= ratio of ablated mass flow rate to input propellant mass flow rate
α	= ablation parameter indicating relative ease of ablating material, $= Q_a/Q_f$ (high α means ablation is difficult)

β	= operating parameter indicating ideal thrust power relative to convective capability of input mass flow, $= (u_i/u_c)^2$ (high β means significant excess thermal power)
ϵ	= fraction of excess thermal power (dissipated power minus power convected by propellant flow) causing ablation

Introduction

FOR several years, it has been suggested that the exhaust velocity of a magnetoplasmadynamic (MPD) arcjet is limited by the so-called Alfvén critical speed¹:

$$u_{crit} = (2E/m)^{1/2} \quad (1)$$

where E is the first ionization level of a fuel atom of mass m . A few theories, based on quite different physical models,^{2,4} have led to this speed as a characteristic value of the exhaust velocity at which electrode erosion, insulator ablation, and/or "plasma instabilities" develop that serve to limit arcjet performance. In particular, for arcjet current J and mass flow \dot{m} , the "onset" of difficulties appears to occur at values of J^2/\dot{m} that result in exhaust speeds near Alfvén critical speed. The present discussion invokes the electromagnetic structure of the discharge flow and a requirement for power balance in steady state in order to derive self-consistent mass flow rates and exhaust speeds. Implications for voltage-current characteristics are described and further research directions are suggested.

Model

The basic equation for the current distribution in a longitudinal plasma flow is

$$\frac{D_r}{Dt} \left(\frac{B}{\rho} \right) = \frac{\nabla^2 B}{\rho \sigma \mu} \quad (2)$$

where ρ is mass density, σ electrical conductivity (assumed constant), and convective derivative is based on the electron fluid velocity u_p . (For high-density flows, the plasma flow velocity \bar{u} may be substituted for u_p .) By dimensional analysis, the characteristic scale over which the magnetic field varies through the plasma flow in steady state is

$$\delta = 1/\sigma \mu u \quad (3)$$

Received Oct. 11, 1985; revision received April 5, 1986. Copyright © 1986 by P. J. Turchi. Published by the American Institute of Aeronautics and Astronautics, Inc., with permission.

*Director

Without flow, the magnetic field would decrease linearly between the upstream and downstream boundaries of the thruster. As the conducting flow accelerates, it convects magnetic flux away from the upstream region and concentrates flux near the downstream ($B=0$) boundary. A bifurcated current density distribution is thereby obtained. Higher flow speeds result in greater current concentration, and more intense dissipation. The consequence of such dissipation is increased ablation of electrodes and insulators. Ablation, however, contributes to the total mass flow rate and thereby lowers the flow speed, reducing the current concentration. A self-consistent solution should therefore be expected.

As a simple model, let convection provide the primary mechanism balancing resistive dissipation, with ablation absorbing the heat not carried away by the fuel mass flow

$$m_A Q_A = \epsilon \{ U^2 \nu / \sigma \} - m_F Q_F \quad (4)$$

where j is the current density, ν the volume in which dissipation occurs, m the mass flow rate, and Q the heat absorbed per unit mass. Subscripts A and F refer to ablated and fuel mass, respectively. The factor ϵ allows energy to be lost without causing ablation (e.g., radiation to free space, thermal conduction).

The current density may be written in terms of the total current J and the characteristic scale δ , which also provides the volume, so

$$U^2 \nu / \sigma = (1/\sigma) (J/2\pi\delta)^2 \pi r^2 \delta g = (\mu/4\pi) J^2 u g \quad (5)$$

where g is a geometric factor that depends on the particular thruster, and u the exhaust speed. The electromagnetic thrust provides this speed:

$$u = (\mu/4\pi) (J^2/m) [\ln(r_2/r_1) + 1/4] \quad (6)$$

where m is the total mass flow rate $m_F + m_A$. Substitution in the equation for ablation results in a quadratic equation:

$$\begin{aligned} (m_F + m_A) \{ m_F Q_F - m_A (Q_A - \epsilon) \} \\ = (\mu/4\pi) J^2 g [\ln(r_2/r_1) + 1/4] \end{aligned} \quad (7)$$

The ablation rate relative to the fuel flow rate is then

$$\Omega = (m_A/m_F) = \{ [(\alpha+1)^2 + 4\alpha(\beta-1)]^{1/2} - (\alpha+1) \} / 2\alpha \quad (8)$$

where $\alpha = Q_A/Q_F$ and

$$\beta = (\mu/4\pi) (J^2/m_F) [g \ln(r_2/r_1) + 1/4] / Q_F \quad (9)$$

For $\beta < 1$, there is no physical solution for the model as constructed. There is insufficient dissipation to account for the heat that could be carried away by the injected mass flow rate absorbing an energy per unit mass Q_F . This insufficiency can be resolved simply by reducing Q_F , i.e., allowing incomplete ionization of the injected flow. For $\beta > 1$, the fuel mass flow cannot cool the thruster sufficiently and ablation occurs. The degree of ablation and thus the exhaust velocity attained for a given current flow depends on the heat that can be absorbed by the ablated material, expressed relative to the fuel by the parameter α .

The condition $\beta = 1$ provides a value for J^2/m_F for which $m_A = 0$ and the dissipation is exactly balanced by convection in the fuel mass flow. This value of J^2/m_F substituted in the equation for exhaust velocity gives

$$u = u_0 = [Q_F g \ln(r_2/r_1) + 1/4]^{1/2} \quad (10)$$

for $Q_F = E/m$ and $g \ln(r_2/r_1) + 1/4 = 2$, $u_0 \approx u_{crit}$. Thus, correlation of self-field plasma thruster performance with Alfvén critical speed might be expected simply on the basis of ablation when the fuel flow rate is insufficient for thruster cooling.

In Fig. 1, the actual speed (i.e., with ablation) is compared with u_0 , the ideal exhaust speed (no ablation), as the ideal speed is increased relative to u_0 . If there is no possibility of ablation ($\alpha = \infty$), then the exhaust speed can increase indefinitely. In the presence of plasma at 1-3 eV, however, solid surfaces can be expected to ablate and ionize about as readily as neutral fuel gas ($\alpha = 1$). Thus, a little excess heating is rapidly compensated by additional mass flow, resulting in an exhaust speed "plateau" at about $u_0 = u_{crit}$.

For $\alpha = 0$, which would correspond to an ablation-fed thruster, Fig. 1 indicates that the exhaust speed decreases relative to u_0 based on Q_F . Proper substitution of this limiting case ($m_F = 0$) in the ablation cooling model, however, provides a constant operating speed

$$u_A = [Q_A g \ln(r_2/r_1) + 1/4]^{1/2} \quad (11)$$

that is basically equivalent to operation at $\beta = 1$. The characteristic discharge thickness for an ablation arc is then

$$\delta_A = (1/\sigma \mu u_A) \quad (12)$$

Incomplete Ionization and Coupling

As noted earlier, the situation of $\beta < 1$ can be associated with incomplete ionization of the input mass flow. If the mean free path for momentum exchange between ions and neutrals is small compared to the discharge and thruster dimensions and the input flow is well mixed into the discharge, then it would be appropriate to divide the electromagnetic thrust by the full mass input rate. The actual exhaust speed should then follow the ideal speed as indicated in Fig. 1 for $\beta < 1$. With poor mixing, however, or at low densities, the ions can slip relative to the neutrals, and the velocity of the electrically conducting fluid can be higher than the ideal speed. In the limit of complete slip, the mass flow subjected to the electromagnetic thrust scales with dissipation. The situation is completely analogous to the pure ablation-fed thruster, with electrical dissipation effectively "ablating" the input neutral mass flow. The conductor speed will be given by:

$$u_C = [Q_C g \ln(r_2/r_1) + 1/4]^{1/2} \quad (13)$$

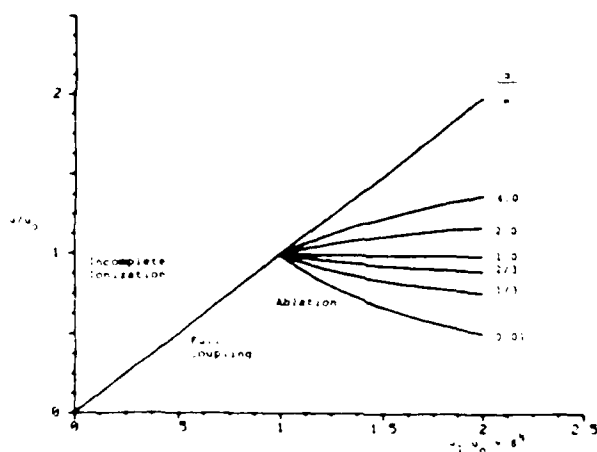


Fig. 1 Variation of actual speed with expected speed, both relative to critical speed u_0 , as a function of energy per unit mass for ablation relative to fuel, $\alpha = Q_A/Q_F$. (Labels refer to regimes of operation discussed in text.)

In the ion slip limit, the ionized fraction of the flow would achieve a high speed at modest current levels and would exhibit constant speed until $\beta = 1$ [which corresponds to complete (single) ionization of the input mass flow].

Voltage-Current Characteristics

To the extent that the voltage across an MPD arcjet largely reflects the electromotive ($u \times B$) effects of plasma flow at significant magnetic Reynolds number, the arcjet voltage-current characteristic should display regimes of operation associated with the velocity of the conducting flow. In Fig. 2, the components of the arcjet voltage are sketched. Anode and cathode falls provide a significant bias that may be nearly constant with respect to total current (although interesting variations, particularly of the anode fall, might be expected). In idealized MPD operation, for which the mass flow is only the input mass flow (no ablation) and a single heavy-particle velocity exists (full ionization and/or no ion slip), the conducting flow speed scales as J , so the voltage $V \sim uB \sim J$. At high current levels ($\beta > 1$) and finite α , however, the mass flow includes ablated material and the speed increases less rapidly with current, perhaps even becoming limited to a constant value. The back EMF component of voltage will then scale linearly with current.

If the input mass flow is not fully ionized and collisionality between ions and neutrals is not sufficient to prevent significant ion slip, then the flow speed that determines the back electromotive force (EMF) will be higher than that computed from the electromagnetic thrust divided by the full input mass flow rate. Since this flow speed will also be constant, scaling with J , the back EMF voltage will increase linearly with J at a level above that for the idealized J variation. Intermediate degrees of collisionality between full slip and complete ion-neutral coupling provide voltage-current characteristics between the linear and cubic variations.

If variations in conductivity and current path length with total current level (and mass flow rate) are ignored compared to the basic variation of discharge thickness with arcjet operation, then two cases can be identified for the resistive component of the voltage. For high magnetic Reynolds number flow, the discharge thickness scales as $(\sigma \mu u)^{-1/2}$, so the resistance will increase as u and the resistive voltage will vary as uJ . This variation will therefore be included in the same manner as the back EMF.

In some regions of the flow, particularly near the propellant inlet, where R_M is low, the current distribution may be determined by processes such as ionization and thermal

transport (i.e., conductivity variations in the direction of the flow are important). If the discharge thickness is constant, for example, then the resistive component of voltage will increase linearly with current and might combine with the back EMF voltage for constant flow speed (due either to incomplete ionization and coupling, or significant ablation).

The total voltage-current characteristic for an MPD arcjet can display a considerable variation depending on the particulars of geometry (e.g., inlet port location and shape) and material selection (α value, collision cross-sections). A linear increase of voltage with current, above constant fall voltages, above constant fall voltages, may be expected at low magnetic Reynolds number and for incomplete ionization and coupling. Transition to cubic variation of voltage with current should then occur as full ionization ($\beta = 1$) is attained, but may be achieved at lower values of current if the magnetic Reynolds number and degree of ion-neutral collisionality are both high. This transition, however, may be obscured if ablation becomes important and the voltage returns to a linear variation with current. Two quite distinct aspects of arcjet design (inlet geometry and insulator material) could thus combine to provide a rather linear voltage-current characteristic for the range of experimental operation.

To the extent that the arcjet current is maintained by the relatively high impedance of the power source, temporal variations in the back EMF component of the voltage reflect similar variations in flow speed. Such flow speed variation affects the current density distribution, i.e., the discharge thickness ($\delta \sim u^{-1/2}$). At high power levels, significant variations in ablation may then occur which in turn result in flow speed variations. As a simple example, suppose that the coupling of dissipation to ablatable surfaces (as expressed by the efficiency ϵ) changes abruptly from $\epsilon = 1$ for a high-speed flow (no ablation) to $\epsilon = 0$, if ablation lowers the flow-speed and thereby broadens the discharge. The arcjet flowfield could then flicker in times scaled by the chamber length divided by the flow speed. Voltage oscillations at a few hundred kilohertz would then be observed (with amplitudes corresponding to the voltage differences between different α values in Fig. 2). Such oscillation in arcjet voltage and flowfield could significantly increase the transport of heat and mass, further degrading performance.

Conclusions

The modeling based on power balance in magneto-plasmodynamic (MPD) arcjet operation is essentially a dimensional argument that indicates scaling relationships. To predict from first principles the detailed behavior of an arcjet of particular geometry, material choice, and propellant type would require a substantially more complex calculational tool, namely a two-dimensional computer code. The present state of the art for such codes is quite sufficient for hydrodynamic calculations including radiation transport, plasma chemistry, and interactions with solid boundaries. Collisionless motion of ensembles of charged particles can also be computed in self-consistent electric and magnetic fields. Estimates of collisional mean free paths vs arcjet dimensions, however, indicate that at least portions of the MPD arcjet operate in a transition flow regime, possibly with nonequilibrium (i.e., evolving) chemistry. Phenomena such as ion slip and incomplete ionization and/or mixing of the injected neutral flow may be inaccessible to both hydrodynamic and collisionless codes.

In lieu of detailed calculations, the present modeling attempts to provide a structure to support understanding of experimental arcjet behavior. Experimental measurements of ion vs neutral velocities as a function of position within the arcjet chamber would be useful to assess the degree of collisionality (and incidentally the degree of ionization). Correlation of collisionality and ionization with overall arcjet behavior (e.g., relationship to onset of noise on voltage

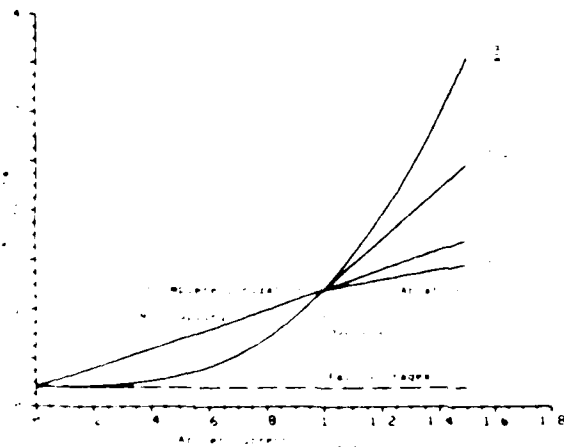


Fig. 2 Sketch of MPD arcjet voltage-current characteristics. Voltage V has arbitrary units and current J is relative to critical current J_{cm} for which $u_f = u_0$ ($J/J_{cm})^2 = u_f/u_0 = \beta^2$. (Labels refer to regimes of operation discussed in text.)

signals) and with variations in chamber geometry, especially the fuel injection arrangement, could then lead to improved criteria for MPD arcjet design.

References

- ¹Alfven, H., "Collision Between a Nonionized Gas and a Magnetized Plasma," *Review of Modern Physics*, Vol. 32, 1960, p. 10.
- ²Malliaris, A. C., John, R. R., Garrison, R. L., and Libby, D. R., "Quasi-Steady MPD Propulsion at High Power," NASA CR-111872, (Avco AVSD-0146-77-RR), Feb. 1971.
- ³Cann, G. L. and Harder, R. L., "Thrust Efficiencies of Electromagnetic Engines," *AIAA Journal*, Vol. 6, March 1968, p. 558.
- ⁴Devillers, P. and Burton, R. L., "The Importance of Alfven's Critical Velocity for MPD Arcs," AIAA Paper 70-1100, 1970.
- ⁵Turchi, P. J., "The Cathode Region of a Quasi-Steady Magneto-plasmdynamic Arcjet," Department of Aerospace and Mechanical Sciences, Princeton University, Princeton, NJ, Rept. AMS 94 OT, Sept. 1970, p. 42.

signals) and with variations in chamber geometry, especially the fuel injection arrangement, could then lead to improved criteria for MPD arcjet design.

References

- ¹Alfven, H., "Collision Between a Nonionized Gas and a Magnetized Plasma," *Review of Modern Physics*, Vol. 32, 1960, p. 710.
- ²Malliaris, A. C., John, R. R., Garrison, R. L., and Libby, D. R., "Quasi-Steady MPD Propulsion at High Power," NASA CR-111872, (Avco AVSD-0146-77-RR), Feb. 1971.
- ³Cann, G. L. and Harder, R. L., "Thrust Efficiencies of Electromagnetic Engines," *AIAA Journal*, Vol. 6, March 1968, p. 558.
- ⁴Devillers, P. and Burton, R. L., "The Importance of Alfven's Critical Velocity for MPD Arcs," AIAA Paper 70-1100, 1970.
- ⁵Turchi, P. J., "The Cathode Region of a Quasi-Steady Magnetoplasmadynamic Arcjet," Department of Aerospace and Mechanical Sciences, Princeton University, Princeton, NJ, Rept. AMS 94 OT, Sept. 1970, p. 42.

END

DATE

FILMED

5-88

DTIC